

The Influence of Muons, Pions, and Trapped Neutrinos on Neutron Star Mergers

Michael A. Pajkos^{1,*} and Elias R. Most^{1,2}

¹*TAPIR, Mailcode 350-17, California Institute of Technology, Pasadena, CA 91125, USA*

²*Walter Burke Institute for Theoretical Physics, California Institute of Technology, Pasadena, CA 91125, USA*

(Dated: September 17, 2024)

The merger of two neutron stars probes dense matter in a hot, neutrino-trapped regime. In this work, we investigate how fully accounting for pions (π), muons (μ), and muon-type neutrinos (ν_μ) in the trapped regime may affect the outcome of the merger. By performing fully general-relativistic hydrodynamics simulations of merging neutron stars with equations of state to which we systematically add those different particle species, we aim to provide a detailed assessment of the impact of muons and pions on the merger and post-merger phase. In particular, we investigate the merger thermodynamics, mass ejection and gravitational wave emission. Our findings are consistent with previous expectations, that the inclusion of such microphysical degrees of freedom and finite temperature corrections leads to frequency shifts on the order of 100 – 200 Hz in the post-merger gravitational wave signal, relative to a fiducial cold nucleonic equation of state model.

I. INTRODUCTION

Neutron star mergers are ideal probes for nuclear matter under extreme conditions [1–4]. Neutron star interiors can reach densities beyond several times nuclear saturation, at which physics beyond those of neutrons (n) and protons (p) can be probed [3, 5]. These can include exotic degrees of freedom such as hyperons [6, 7] or deconfined quarks [8, 9], but also mesons, including pions (π^\pm) [10–12]. Revealing this complex and intricate interplay of the physics of the strong interaction is at the core of modern astrophysical neutron star research. As such, various ways have been proposed and investigated to reveal matter under extreme conditions in neutron stars. These range from X-ray observations of neutron star cooling curves and hotspots on neutron stars [5, 13], which has yielded novel constraints on the dense matter equation of state [14–18], especially when combined with advances in chiral effective field theory descriptions of nuclear matter around saturation [19].

Within the realm of gravitational wave astrophysics, detections of gravitational waves from merging neutron stars [20, 21] have the potential to directly probe and constrain dense matter physics, including finite temperature effects [22]. The inspiral part of the gravitational waveform can constrain neutron star radii and the cold equation of state [23, 24], with remarkable constraints obtained from the first neutron star merger event GW170817 (e.g., [25–29], see also [30–38]). With next-generation facilities, future detections of post-merger gravitational waves have the potential to detect the kilohertz oscillations of the neutron-star merger remnant formed in intermediate and low mass mergers [39, 40]. These frequencies are quasi-universally related to properties of the dense matter equation of state [41–49] (see also [50] for bounds on this universality). The post-merger phase probes higher densities and

temperatures than present in the inspiral, and could reveal the appearance of quark matter [51–58], hot dense matter [59–67], hyperons [68–70] and neutrinos [71–75], fueling effective chemical reactions inside the merger remnant. While the latter could in principle affect the outcome of the merger via an effective viscosity [72], the strength of the effect depends strongly on the neutrino conditions and opacity [74, 75]. In particular, it has been found that likely the remnant will be optically thick to neutrino emission, leading to an effective trapping of neutrinos and to a correction of the equation of state [74]. This neutrino trapped regime can depend crucially on the microphysical interactions included [76], including through the appearance of muons (μ^\pm) and pions, π^\pm [77] (see also [78]). Recent numerical studies have further been aimed at quantifying the impact of these particles independently [79, 80]. Similar conclusions have also been found for core-collapse supernovae, where the inclusion of muons and pions may critically affect the explosion mechanism [81–83].

Recent works in the field have made substantial progress towards quantifying the effects of additional particles. Ref. [80] varies the mass of the pion and quantifies the characteristics of the NSNS dynamics and resulting GW signal. Ref. [79] uses an advanced postprocessing scheme to quantify the changes in pressure in the presence of muons and trapped neutrinos, finding changes in pressure of order 10%. More recently, Ref. [84] allows for the advection of muons, paired with a neutrino leakage scheme.

Building upon these works, we perform fully general-relativistic neutron star merger simulations, which model the influence of mesons, such as pions (π^\pm) in their thermal and condensed state, and leptons, such as muons (μ^\pm) and (anti)neutrinos (ν) in the fully trapped regime. We then analyze the impact on the merger dynamics, gravitational wave emission, and mass ejection from the system.

Our work is organized as follows, in Section II A

* E-mail: mpajkos@caltech.edu

we outline the relevant particle processes we choose to model. Section II B provides the statistic description of the various particles. Section II C we outline the relevant steps to update nuclear EOS to include these particles for the NSNS system, with more detail in Appendix A. Section II D provides thermodynamic contributions from each species. Section II E introduces the EOSs used in this work. Section II F describes the general properties of the newly constructed EOSs. Section II G quantifies the impact of different species on isolated NSs. Section II H details the numerical tools in this work. Section III describes our simulation results. Lastly, Section IV concludes.

Unless otherwise noted, in this work we adopt units $G = c = 1$, where G is the gravitational constant, and c the speed of light.

II. METHODS

In the following, we outline the construction of the equation of state, as well as the setup for our numerical simulations.

A. Particle Processes

We begin by discussing the main particle interactions of muons and pions relevant to neutron star mergers. Our presentation largely follows that of Refs. [79, 80].

The principal decay channel of a charged pion (π^\pm , with bare mass $m_\pi \sim 140$ MeV) into charged muons, μ^\pm , is as follows,

$$\pi^- \leftrightarrow \mu^- + \bar{\nu}_\mu, \quad (1)$$

where $\bar{\nu}_\mu$ denotes a muon anti-neutrino. Charged $\bar{\nu}_\mu$ (with bare mass $m_\mu \sim 106$ MeV) will further decay into electrons, e^- , electron type antineutrino, $\bar{\nu}_e$, and muon type neutrino, ν_μ ,

$$\mu^- \leftrightarrow e^- + \bar{\nu}_e + \nu_\mu. \quad (2)$$

The last relevant reaction is neutron (n , with bare mass $m_n \sim 940$ MeV) decay into a proton (p), electron, and electron type antineutrino

$$n \leftrightarrow p + e^- + \bar{\nu}_e. \quad (3)$$

We now assume that neutrinos inside the neutron star merger remnant are trapped [74], and therefore approximate weak decays inside the hot and dense merger remnant [60], as being in weak-interaction equilibrium. As a result, we can equate the reactions in terms of their chemical potentials, μ_i ,

$$\mu_{\pi^\mp} = \mu_{\mu^\mp} - \mu_{\nu_\mu} = \mu_{e^\mp} - \mu_{\nu_e} = \pm(\mu_n - \mu_p), \quad (4)$$

where the different signs correspond to negatively and positively charged current reactions, respectively. Apart

from weak-interaction equilibrium, we also need to account for charge neutrality. As a result, the overall particle fractions, $Y_i = n_i/n_b$, where n_i are the particle number densities and n_b is the baryon number density, obey

$$Y_p = Y_e + Y_\pi + Y_\mu, \quad (5)$$

where $Y_e = Y_{e^-} - Y_{e^+}$, $Y_\pi = Y_{\pi^-} - Y_{\pi^+} + Y_\pi^c$, and $Y_\mu = Y_{\mu^-} - Y_{\mu^+}$. Here Y_π^c accounts for the presence of a negatively charged pion condensate. Particles that follow Bose-Einstein statistics can form multiple particles in the same quantum state at the lowest energy level of the system. These particles have rest mass, but no kinetic energy, and do not contribute pressure to the surrounding system. As such, we call pions which do not condense (Y_{π^-}, Y_{π^+}) *thermal* pions. Neutral pions (π_0) are added by assuming a vanishing chemical potential, $\mu_{\pi_0} = 0$.

Similar to Ref. [79], we define the lepton fraction for a species i , described as

$$Y_{l,i} = (Y_{i^-} - Y_{i^+}) + Y_{\nu_i} - Y_{\bar{\nu}_i} \mid i \in \{e, \mu\}. \quad (6)$$

One central assumption to our work is that the electron lepton number in the simulation is advected along with the fluid [60, 85],

$$u^\mu \nabla_\mu Y_{l,e} = 0, \quad (7)$$

where u^μ is the fluid four-velocity, which is in good agreement with neutrino transport simulations of neutron star mergers [74]. $Y_{l,\mu}$ is chosen to be a constant of 0.01 below a density threshold of 10^{14}g cm^{-3} . Above this threshold, it is parameterized as a function of density $Y_{l,\mu}(\rho)$. For a detailed explanation of our choice of $Y_{l,\mu}$, see Appendix A.

B. Statistical Descriptions of Pions and Muons

In order to describe muon and pion corrections to the equation of state, we need to translate Eqs. (4) and (5) into corrections of the energy density and pressure of the equation of state. As an intermediate step, this involves computing the particle fractions of e^\pm , μ^\pm , π^\pm , ν_i , and $\bar{\nu}_i$. We will also provide the expressions for the number density, n_i , of the respective particles.

1. Muons and Electrons

Leptons ($l = \mu, e$) are treated as an ideal Fermi gas whose number density can be described as (Equation (16) of [79]),

$$n_{l^\pm} = K_l \theta_l^{3/2} \left[F_{1/2}(\eta_{l^\pm}^\pm, \theta_l) + \theta_l F_{3/2}(\eta_{l^\pm}^\pm, \theta_l) \right], \quad (8)$$

for $K_l = 8\sqrt{2}\pi(m_l c^2/hc)^3$, $\theta_l = k_B T/(m_l c^2)$, $\eta_{l^\pm}^\pm = (\mu_{l^\pm} - m_l c^2)/(k_B T)$, F_k are Fermi functions of order k ,

m_l is the mass of the lepton, and h and k_B are Planck's and the Boltzmann constant, respectively. These Fermi functions are defined as (Equation (6) of [86])

$$F_k(\eta, \theta) = \int_0^\infty dx \frac{x^k \sqrt{1 + 0.5\theta x}}{e^{x-\eta} + 1}. \quad (9)$$

2. Pions

Pions, by contrast, are treated as a free Bose gas. Note, the use of μ in this section refers to chemical potential, rather than muons. As a Bose gas, the pion number density is given by [87],

$$n_\pi = \frac{1}{\lambda^3} g_{3/2}(z) = \frac{1}{\lambda^3} \frac{2}{\sqrt{\pi}} \int_0^\infty dy \frac{y^{1/2}}{z^{-1}e^y - 1}, \quad (10)$$

where $\lambda = (h^2/2\pi m k_B T)^{1/2}$ and the fugacity is $z = e^{\mu/(k_B T)} = e^{(\tilde{\mu}-m)/(k_B T)}$; for the corresponding antiparticle, $z = e^{(-\tilde{\mu}-m)/(k_B T)}$. The integral in Equation (10) can be approximated with an infinite series, simplifying to

$$n_\pi = \frac{1}{\lambda^3} \left(z + \frac{z^2}{2^{3/2}} + \frac{z^3}{3^{3/2}} + \dots \right). \quad (11)$$

We follow the nomenclature of [88] where $\tilde{\mu}$ is the chemical potential of the particle with the rest mass included, and μ is the chemical potential without the particle rest mass; concretely, $\mu_i = \tilde{\mu}_i - m_i$.

As an important note for pions, if $\tilde{\mu} > m_{\pi^-}$ a negatively charged pion condensate (π_c^-) will form. In regions of our simulation where this is the case, to populate the *thermal* pions, π^- one follows the above Bose-Einstein statistics, with a chemical potential of the thermal pion equal to the charged pion rest mass, $\tilde{\mu}_{\pi^-} = m_{\pi^-}$. To calculate the number density of the condensate, one must follow a more detailed procedure in Appendix A, that relies on balancing charge neutrality.

3. Neutrinos

In this work, we assume that neutrinos are trapped through the neutron star merger remnant, which is consistent with recent simulations using full neutrino transport [74]. In the neutrino trapped regime, neutrinos behave as a massless Fermi gas, whose number density can be described as [79],

$$n_\nu = \frac{4\pi}{(hc)^3} (k_B T)^3 F_2(\eta_\nu) \exp(-\rho_{\text{lim}}/\rho) \quad (12)$$

where $\exp(-\rho_{\text{lim}}/\rho)$ is an exponential damping factor [89] to model trapped neutrinos above $\rho_{\text{lim}} = 10^{14} \text{ g cm}^{-3}$.

Here, the degeneracy parameter of the neutrinos is calculated as

$$\eta_{\nu_l} = (\mu_p - \mu_n + \mu_l)/k_{\text{B}}T \quad (13)$$

and $\eta_{\bar{\nu}} = -\eta_\nu$. In practice, these enter our calculation via the net number fraction of neutrinos, represented by $Y_\nu - Y_{\bar{\nu}} \propto n_\nu - n_{\bar{\nu}}$. Applying Equation (12), we use the exact expression provided by [89]

$$Y_\nu - Y_{\bar{\nu}} \propto F_2(\eta_\nu) - F_2(-\eta_\nu) = \frac{1}{3} \eta_\nu (\pi^2 + \eta_\nu^2) \quad (14)$$

which provides a more accurate expression of the net number density, without numerical integration of Fermi integrals $F_2(\eta_\nu)$.

C. Equation of State

Armed with the statistical descriptions for the number density for each species, we now outline our methodology to populate a given equation of state with each new particle. Begin with charge conservation for the proton fraction

$$Y_p = Y_e + Y_\mu + Y_\pi. \quad (15)$$

Likewise, we assert lepton number conservation for species of electrons and muons

$$Y_{l,e} = Y_e + Y_{\nu_e} - Y_{\bar{\nu}_e} \quad (16)$$

and

$$Y_{l,\mu} = Y_\mu + Y_{\nu_\mu} - Y_{\bar{\nu}_\mu}. \quad (17)$$

Combining the previous three equations we yield,

$$\hat{Y}_p = Y_{l,e} - (Y_{\nu_e} - Y_{\bar{\nu}_e}) + Y_{l,\mu} - (Y_{\nu_\mu} - Y_{\bar{\nu}_\mu}) + Y_\pi. \quad (18)$$

Here \hat{Y}_p indicates our iteration variable of choice that will eventually converge to $Y_{p,\text{new}}$ for our updated equation of state.

Equation (18) provides a modular framework to add particles to the system. In our work, we create three new variants by modifying the *base* equation of state. The first variant purely accounts for electron type (anti)neutrinos, the $+\nu_e$ case. The $+\nu_e$ case zeros out the $Y_{l,\mu}$, $(Y_{\nu_\mu} - Y_{\bar{\nu}_\mu})$, and Y_π terms. The second variant accounts for electron type (anti)neutrinos and pions, the $+\nu_e + \pi$ case. This variant zeros out the $Y_{l,\mu}$ and $(Y_{\nu_\mu} - Y_{\bar{\nu}_\mu})$ terms. The third variant accounts for electron type (anti)neutrinos, pions, muons, and muon type (anti)neutrinos, the $+\nu_{e,\mu} + \pi + \mu$ case. This variant includes all terms in Equation (18). In Appendix A, we enumerate our procedure, in detail, to add the new particle species to the EOS.

D. Calculating Thermodynamic Quantities

Having calculated the charge fractions (or number densities) of pions and muons, we can calculate the pressure, P , and specific internal energy, ϵ , of the pions, muons, and trapped neutrinos. In the following sections, we list the expressions for energy density, that has units of energy per volume. To convert the energy density expressions to specific internal energy, simply divide by the rest mass density $\epsilon_{\mu/\pi} = \varepsilon_{\mu/\pi}/\rho$.

1. Pions

For pions, we leverage Bose-Einstein statistics. For the pressure,

$$P_{\text{Bose}} = g_{5/2}(z(T)) \left(\frac{2\pi m_{\pi}}{h^2} \right)^{3/2} (k_{\text{B}}T)^{5/2}, \quad (19)$$

where $g_{5/2}(z(T))$ can be described as

$$g_{5/2}(z(T)) = \frac{1}{\Gamma(5/2)} \int_0^{\infty} dy \frac{y^{3/2}}{z^{-1}e^y - 1}. \quad (20)$$

Note, $\Gamma(5/2) = 3\sqrt{\pi}/4$ and $g_{5/2}(z = 1) = \zeta(5/2) \sim 1.342$. For the energy density [90], $\varepsilon_{\text{Bose}} = \frac{3}{2}p_{\text{Bose}} + n_{\pi}m_{\pi}c^2$. Note the additional contributions from the rest mass, $n_{\mu}m_{\mu}c^2$.

2. Muons

For muons, we leverage Fermi-Dirac statistics [79, 91]. For pressure,

$$P_{\mu^{\pm}} = \frac{1}{3}K_{\mu}m_{\mu}c^2\theta_{\mu}^{5/2} \left[2F_{3/2}(\eta'_{\mu^{\pm}}, \theta_{\mu}) + \theta_{\mu}F_{5/2}(\eta'_{\mu^{\pm}}, \theta_{\mu}) \right]. \quad (21)$$

For the energy density,

$$\begin{aligned} \varepsilon_{\mu^{\pm}} &= K_{\mu}m_{\mu}c^2\theta_{\mu}^{5/2} \left[F_{3/2}(\eta'_{\mu^{\pm}}, \theta_{\mu}) + \theta_{\mu}F_{5/2}(\eta'_{\mu^{\pm}}, \theta_{\mu}) \right] \\ &+ n_{\mu}m_{\mu}c^2. \end{aligned} \quad (22)$$

Note, the last term in the equation accounts for contributions from the rest mass of the muons.

3. Neutrinos

We treat neutrinos as a massless Fermi gas [79]. For the energy density,

$$\varepsilon_{\nu} = \frac{4\pi}{(hc)^3} (k_{\text{B}}T)^4 F_3(\eta_{\nu}) \exp(-\rho_{\text{lim}}/\rho) \quad (23)$$

where the term $\exp(-\rho_{\text{lim}}/\rho)$ is used to smoothly cutoff neutrino trapping above $10^{14} \text{ g cm}^{-3}$ [92]. Note, in practice, the calculations of $F_3(\eta_{\nu})$ can be cumbersome. However, since we are interested in the contributions from antineutrinos as well, the expressions for the net energy density from neutrinos and corresponding antineutrinos becomes

$$\varepsilon_{\nu} + \varepsilon_{\bar{\nu}} \propto F_3(\eta_{\nu}) + F_3(-\eta_{\nu}) = \frac{7\pi^4}{60} + \frac{1}{2}\eta^2(\pi^2 + \frac{1}{2}\eta^2), \quad (24)$$

where in the last expression, we make use of the properties of sums of Fermi integrals [93]. This expression both simplifies computation and is more precise than performing numerical integration. The expression for pressure simply follows from that of an ultrarelativistic gas,

$$P_{\nu} = \varepsilon_{\nu}/3. \quad (25)$$

E. Equation of State Models

In order to apply pion and muon corrections, we need to adopt an underlying equation of state framework. We here adopt two models, SFHo [94] and DD2 [95–97] EOSs. The calculations used in both EOSs are based on a relativistic mean field model for nucleons. Both unmodified tables tabulate basic thermodynamic quantities (e.g., pressure or speed of sound) against three independent variables (ρ, T, Y_p). These tables assume nuclear statistical equilibrium (NSE) among the constituent particles: nuclei, nucleons, electrons, positrons, and photons. For these unmodified tables, only the protons, electrons, and positrons are assumed to contribute to the charge fraction, or $Y_p = Y_{e^-} - Y_{e^+}$. As outlined in the Appendix A, we detail our procedure to create tabulated EOSs against ($\rho, T, Y_{l,e}$).

Corrections for pions and muons are applied to the entirety of the new EOS table, whereas EOS contributions from trapped neutrinos are only added in the regime roughly above the neutrino trapping limit of $10^{14} \text{ g cm}^{-3}$ due to the exponential damping factor of $\exp(-\rho/\rho_{\text{lim}})$ in Equation (24). Ideally, this approximation to neutrino trapping should not be used during the inspiral phase of the merger because there are no expected neutrino contributions from isolated NS companions. Because we do not see major neutrino fractions in the isolated companions, and for the simplicity of a single EOS table during the entire evolution, we employ this approximation.

F. General Equation of State Properties

In this Section, we present general properties of the ν_{e^-} , μ^- , and π -augmented equation of states, including

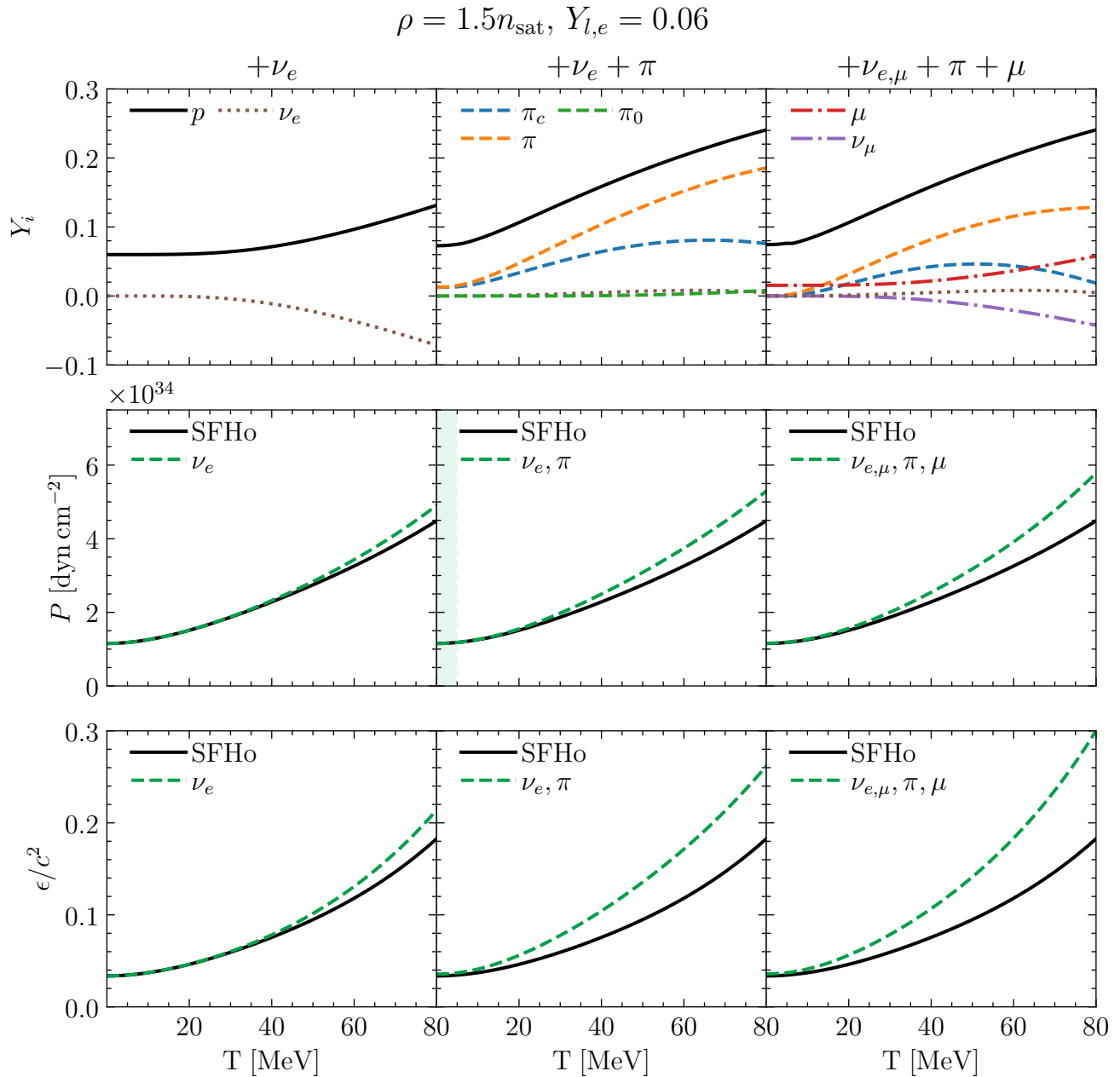


FIG. 1: Physical quantities for the SFHo EOS, taken at rest-mass density $\rho = 3.9 \times 10^{14} \text{ g cm}^{-3}$ and lepton fraction $Y_{l,e} = 0.02$. The left column represents only electron type (anti)neutrinos (ν_e). The middle column represents ν_e and pions (π) (including condensed pions, π_c). The right column includes ν_e , π , muons μ , and muon (anti)neutrinos (ν_μ). (Top row) Particle fractions for various species. (Middle row) Pressure, P , as a function of temperature, T , for the unmodified SFHo equation of state and SFHo with additional particles. The shaded region represents where the pressure $P_{\text{SFHo}} > P_{+\nu_e+\pi}$. (Bottom row) Specific internal energy, ϵ , as a function of temperature.

particle fractions, pressure profiles, and specific internal energy profiles. We begin our analysis to look at general properties of the EOS by investigating estimates for particle fractions Y_i under typical thermodynamic conditions in the merger. These plots are generated for typ-

ical conditions found in a neutron star merger remnant [60, 98], $\rho = 1.5n_{\text{sat}} = 3.9 \times 10^{14} \text{ g cm}^{-3}$, $Y_{l,e} = 0.06$, and $0.01 \lesssim T \lesssim 80 \text{ MeV}$. These calculations are presented in Figure 1 and Figure 2 for the SFHo and DD2 EOS, respectively.

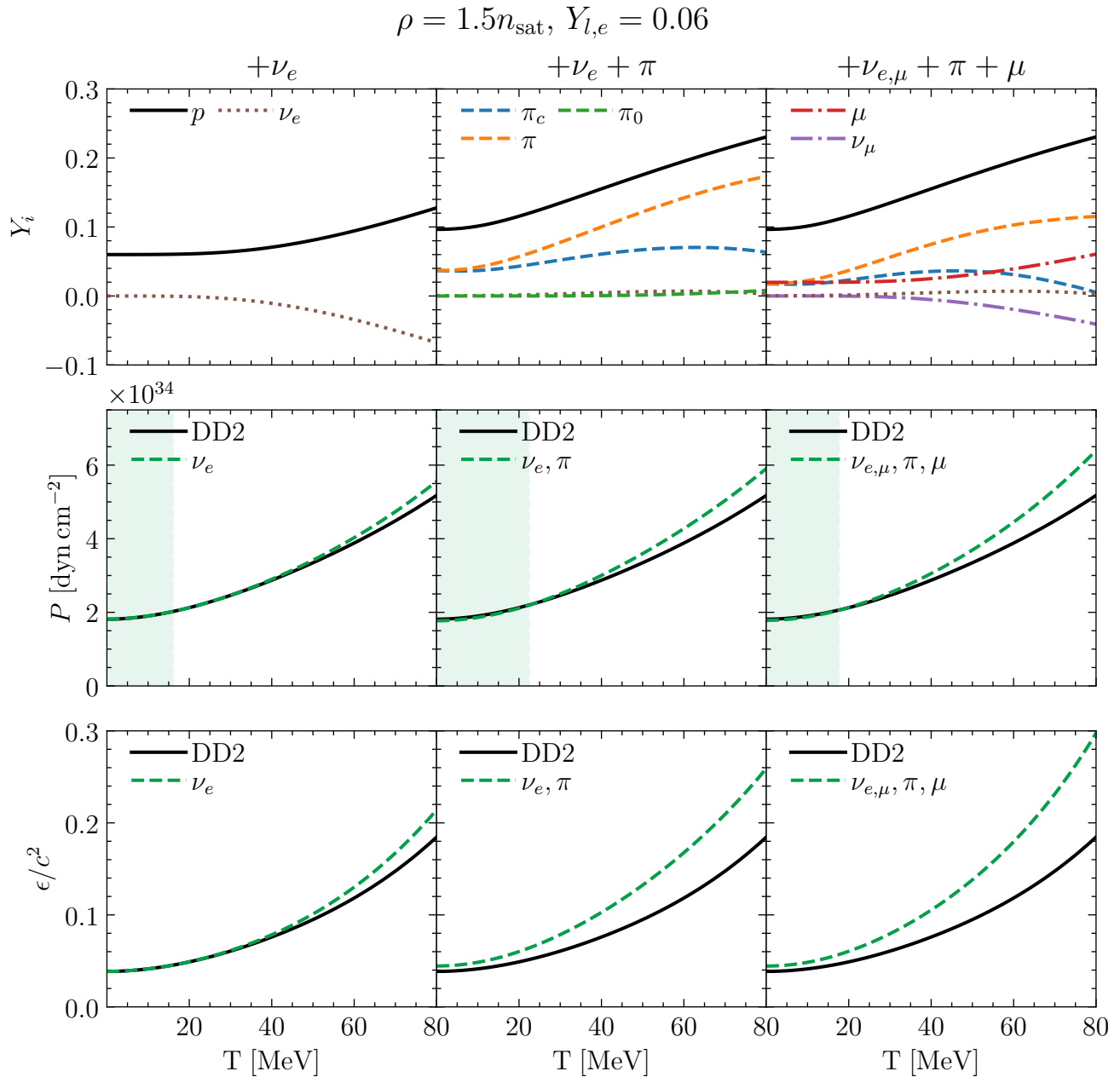


FIG. 2: Same as Figure 1, but for the DD2 EOS.

Begin by examining the top left panel of Figure 1. We see the particle fractions for protons (Y_p) and electron type neutrinos Y_{ν_e} . Recall in this work, we define Y_{ν_e} (and similarly $Y_{\nu_{\mu}}$) as the difference of the particle fraction of the neutrinos with the particle fraction of the corresponding antineutrinos, Equation (17). This definition implies that negative values of Y_{ν_e} signify the presence of more antineutrinos than neutrinos. At low temperatures, there is no noticeable imbalance between neutrinos and antineutrinos. With increasing temperature, there

is an increasing imbalance, indicated by $Y_{\nu_e} \sim -0.07$ at $T = 80$ MeV. The Y_p behavior is characterized by a steady increase with temperature from $Y_p = 0.06$ to $Y_p \sim 0.13$. This behavior is defined by Equation (16). Since the table is defined at a fixed $Y_{l,e} = 0.06$, as Y_{ν_e} steadily decreases, Y_e , and thus Y_p , must steadily increase.

In the middle panel of the first row, we additionally examine pion-related quantities for the $+\nu_e + \pi$ case. The newly labeled quantities are condensed pions (Y_{π_c}),

thermal and condensed charged pions (Y_π), and thermal neutral pions Y_{π_0} . At lower temperature values, the dashed orange line displays values around 0.04 for Y_π . This is due to pion condensate forming. As temperatures increase, the thermal population of pions increases. By contrast, the condensate does not increase as rapidly. Thus, Y_{π_c}/Y_π is decreasing as temperature increases. This behavior represents pions moving from the lowest available energy state into higher energy levels, due to increased temperature. At $T = 80$ MeV, we see $Y_{\pi_c} \sim 0.08$ and $Y_\pi \sim 0.18$. There is a moderate increase in Y_{π_0} due to thermal effects. Note the drastically different behavior of Y_{ν_e} . In contrast with the $+\nu_e$ case, Y_{ν_e} remains close to 0. This is a direct consequence of pion condensation via Equation (4). Because μ_π is bounded by m_π , and the pions are in strong equilibrium with the baryons, $\mu_n - \mu_p$ is also limited by m_π . This in turn limits η_{ν_e} , limiting the imbalance between electron neutrinos and antineutrinos. As a consequence of these low Y_{ν_e} values, notice the similar shape of Y_p (solid black line) and Y_π . These two curves are shifted by the $Y_e \sim Y_{l,e} \sim 0.06$, as a result of Equation (5).

In the right panel of the first row, we additionally examine muon-related quantities for the $+\nu_{e,\mu} + \pi + \mu$ case. At low temperatures, in the dashed - dot red line, we see a $Y_\mu \sim 0.02$ —and at temperatures near 80 MeV—climbing to $Y_\mu \sim 0.06$. This behavior is justified as higher temperatures increase the total available amount of thermal energy to produce new particles. At lower temperatures, there is no noticeable imbalance between muon type neutrinos and muon type antineutrinos. However, at higher temperatures, we see $Y_{\bar{\nu}_\mu} \sim -0.04$. Similar to before, Y_μ and $Y_{\bar{\nu}_\mu}$ mirroring each other is a direct consequence of Equation (17). In this regime, $Y_{l,\mu}$ remains constant, so the sum of both dashed-dot lines remains a constant as well. Compared to the $+\nu_e + \pi$ case, at all temperatures, Y_π (dashed line) has shifted to lower values because of the increased presence of charged μ , limiting the total available charge for pion condensate to form. Furthermore, notice Y_{π_c} is clearly non monotonic near the upper end of the temperatures. In this regime, the formation of $\bar{\nu}_\mu$ drives up the production μ , in order to keep $Y_{l,\mu}$ constant. With an increasing Y_μ , the condensed population of pions cannot form as prolifically, forcing Y_{π_c} to decrease more quickly.

One clear observation is that Y_p displays similar behavior between the $+\nu_e + \pi$ and $+\nu_{e,\mu} + \pi + \mu$ cases. This feature is a consequence of the formation of a pion condensate (see Appendix A 3 for a discussion about pion condensation). In particular, Y_p is determined for a given ρ , T , $Y_{l,e}$ when the difference in chemical potentials between neutrons and protons exceeds the charged pion mass, or $\mu_n - \mu_p \geq m_{\pi^-}$. Physically, this expression implies, in the presence of condensate, that the charge fraction is limited by the mass of the pion. How much condensate forms will be limited by the amounts of other charge carriers: muons and electrons, both of which are affected by the presence of neutrinos.

The left column in the middle row shows the pressure contributions in the $+\nu_e$ case. At lower temperatures, the pressures are nearly identical because there is no significant production of ν_e . Only at higher temperatures, with increasing production of (anti)neutrinos, do more noticeable deviations occur, around the 10% level.

The middle column, middle row shows pressures for $+\nu_e + \pi$. At low temperatures, the pressure is slightly lower when pions are included, compared to the base EOS. This is indicated by the green shaded region. These results are in line with Ref. [80]. This behavior is due to the fact that the increased presence of pions creates a larger proton fraction, compared to before. At this density and $Y_{l,e}$, the pressure reaches a minimum at $Y_p \sim 0.08$. Thus, the higher charge fraction near 0.1 is conducive to lower pressures. Furthermore, the majority of pions at lower temperatures are condensate; they will not contribute to the pressure of the EOS. At higher temperatures, the increased presence of thermal pions provides additional pressure, with the $+\nu_e + \pi$ case displaying higher pressures at $\gtrsim 5$ MeV. In the middle row, right column, we notice the shaded region is removed. This feature indicates the pressure is higher than the base EOS for the $+\nu_{e,\mu} + \pi + \mu$ case. While $Y_p(T)$ is similar for both EOS variants, the key difference is the increased presence of muons and ν_μ . These particles are an additional source of pressure, causing slightly higher pressures at all temperatures, compared to the control EOS.

The lower left plot displays the specific internal energy, normalized by the speed of light squared, as a function of temperature. At low temperatures, we see the $+\nu_e$ case only marginally higher than the base EOS. Similar to the pressure, only at higher temperatures does the increase in ϵ become apparent, reaching differences around the 20% level at the $T = 80$ MeV.

In the bottom row, middle column, we see ϵ behavior in contrast to [80], who see a lower energy density than the base EOS. In our EOS table, at $\rho = 1.5n_{\text{sat}}$ and $T = 1$ MeV, we observe the behavior of ϵ as a function of Y_p . We see a minimum in ϵ at $Y_p \sim 0.06$. As Y_p increases beyond that, so too does ϵ . This gives a $+\nu_e + \pi$ line higher than our control SFHo. At higher temperatures, the $+\nu_e + \pi$ EOS continues to deviate from the base EOS as the energy contributions from the additional pion species create a larger ϵ . In the last panel, the presence of muons increases the specific internal energies at higher temperatures through the existence of other species of muons and neutrinos.

Between both EOSs, both Figure 1 and Figure 2 display similar qualitative behavior, with differences in the numerical values because of different stiffnesses of each EOS. A noteworthy feature in Figure 2 is the middle row describing the DD2 pressures. The shaded regions, where the modified pressure is lower than the control pressure, are present for all three modifications of the EOS. As new species are added, the temperature at which the modified pressure exceeds the control pressure varies from ~ 16

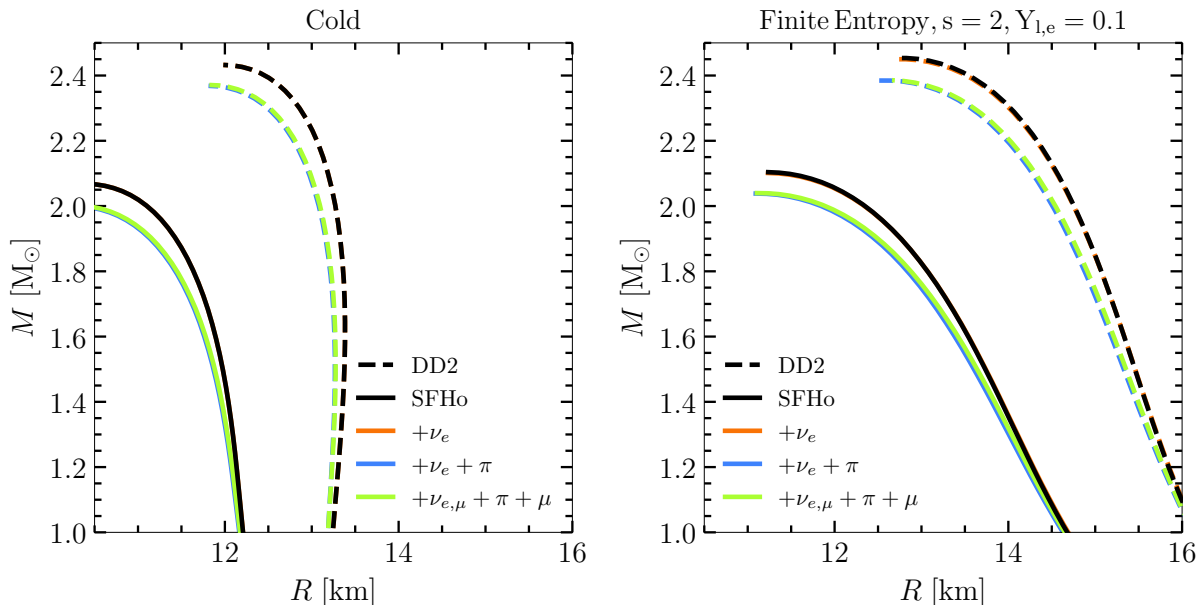


FIG. 3: Mass (M)-radius (R) curves for non-rotating neutron stars. Shown are results for the DD2 and SFHo equations of state. The left column assumes cold β -equilibrium, and the right column assumes constant entropy of $s = 2k_B$ /baryon at constant $Y_{l,e} = 0.02$. For all cases, the addition of pions (π) and muons (μ), and trapped electron neutrinos (ν_e) softens the EOS and creates smaller, less massive NSs.

MeV to ~ 22 MeV to ~ 17 MeV for the $+\nu_e$, $+\nu_e + \pi$, and $+\nu_{e,\mu} + \pi + \mu$ cases, respectively. For $+\nu_e$ we do not expect this green shaded region, representing a pressure drop, to be dynamically relevant, because of the lack of ν_e in this low temperature regime. The presence of pions in the middle panel produces a larger shaded region because of the formation of pressureless condensate. The green shaded region in the right panel moves to lower temperatures because the additional muonic species provide additional pressure support, shifting the dashed green curve upwards. In the lowest row, the behavior of ϵ behaves similar to SFHo.

G. Influence on Isolated Neutron Stars

To translate the changes in microphysics into macroscopic observables, we first construct cold, non-rotating neutron star solutions in weak-interaction (β -) equilibrium. To address the influence of neutrinos in a higher temperature scenario, we consider finite entropy, constant $Y_{l,e}$ NSs.

By solving the Tolman-Oppenheimer-Volkoff (TOV) equations [99, 100] for a variety of initial central densities, we construct mass-radius curves (Figure 3). To construct these, we slice our finite temperature EOS for a variety of ρ values, at a low temperature $T = 0.1$ MeV, imposing β -equilibrium: $\mu_n - \mu_p = \mu_e$. Note, we do not account for the neutrino chemical potential because trapped neutrinos are not prevalent at low temperatures.

These ‘cold’ TOV stars are seen in the left panel of Figure 3.

As expected for the cold case, including ν_e creates a mass-radius curve directly under the unmodified EOS results. At this low temperature, there are not sufficient neutrinos to modify the NS structure, supported by the middle row, left panel of Figure 1. The inclusion of pions leads to an overall reduction in pressure, causing the EOS to soften considerably. As suggested in the middle row of Figure 1, high density, low temperature environments will form pion condensate. This translates to overall lower maximum masses in the EOS including pions, seen in the blue lines of Figure 3. Lastly, at marginally higher mass and radii, the $+\nu_{e,\mu} + \pi + \mu$ case (in lime green) behavior is justified by the additional pressure from muons.

Indeed, the post-merger remnant will have a region of high temperature in a ring structure around the center. To approximate relatively higher temperature in the interior of the star, compared to the outer atmosphere, we also construct beta equilibrium, finite entropy TOV stars, displayed in the right panel of Figure 3. To construct these, we begin with our EOS variants. For a variety of densities, we select points that have entropies of $s = 2k_B$ /by and have a constant $Y_{l,e} = 0.1$, coarsely representative of the remnant. While muons do not appreciably change the mass radius, the impact of trapped muon neutrinos, ν_μ , has been argued to affect the post-merger dynamics [79]. Trapped neutrinos only become relevant at high temperatures, as can be seen by the

(small) changes in the mass radius curve when considering fixed specific entropy models, just below the black curves. Similar to the cold TOV case, the presence of pions (specifically the condensate) has the largest impact on the structure of the mass-radius curves.

H. Numerical Methods

To process our EOS data, we use the ‘stellar collapse’[101] format, using a python analysis script. Once our new EOSs are obtained, we solve the TOV equations using a publicly available solver [102].

In this work, we also present results of neutron star merger simulations in full numerical relativity. To this end, we solve the equations of general-relativistic (magneto-)hydrodynamics (GRMHD) in dynamical spacetimes [103]. We model the spacetime dynamics using the Z4c formulation of the Einstein equations [104, 105]. The combined set of equations is solved using the Frankfurt/IllinoisGRMHD (FIL) code [106, 107]. FIL is based on the EinsteinToolkit infrastructure [108], and provides high-order conservative finite-difference methods for the GRMHD equations [109] and an unlimited fourth-order discretization for the spacetime equations [110]. More specifically, FIL implements a fourth-order version of the ECHO scheme [109] using WENO-Z reconstruction [111], and provides its own infrastructure for handling tabulated equations of state and primitive inversion using the method of [112]. The computational domain is handled using the Carpet fixed mesh-refinement infrastructure [113]. In particular, we use 7 levels of moving mesh refinement with a finest resolution $\Delta x = 260\text{m}$. The outer boundaries are placed at a distance of 3,000 km. The choice of resolutions is consistent with FIL’s beyond second-order convergence [106], see also Refs. [51, 53, 75, 114] for similar studies of nuclear matter effects with the code.

We generate numerical initial conditions using the Kadath[115]/FUKA[116] set of codes, which solve the extended conformal thin sandwich formulation [117]. We neglect initial neutron star spins (see [118], and also Refs. [119–121] for simulations studying the impact of spins with the code) and model the neutron stars as irrotational. We consider initial neutron star masses, $m_1 = 1.25M_\odot$ and $m_2 = 1.25M_\odot$ at a separation of 45 km.

III. SIMULATION RESULTS

Following the construction of our augmented equation of state models, we now investigate their impact on fully general-relativistic neutron star merger simulations.

A. Merger Dynamics and Remnant Composition

Having identified how the initial conditions of the individual neutron stars will change, we transition to describing where in the merger and post-merger these species should occur and how this region changes throughout the evolution of the system. To provide a picture of the merger remnant, we focus on Figure 4. The right half of each panel shows the electronic lepton fraction, $Y_{l,e}$. Owing to initial weak-interaction equilibrium, the system commonly features low $Y_{l,e}$ cores and relatively higher $Y_{l,e}$ outer disk material. For all cases, we see a high temperature ring up to 40(30) MeV off-center for SFHo (DD2). We can see that the addition of π leads to a small reduction in overall temperatures. Likewise, we provide density contours at n_{sat} and $2n_{\text{sat}}$, seen in black. This reveals that the SFHo merger with π is slightly more compact. This remnant picture will be useful in describing the particle fractions for the new species. Differences in the structure of the temperature profiles will be discussed in Section III B.

Figure 5 describes the particle fractions of the negatively charged thermal pions, positively charged thermal pions, and pion condensate. Due to the low temperature in the inspiral, the initial NSs prior to merger feature only small amounts of (thermal) pions, $Y_{\pi^-} \lesssim 10^{-2}$. The merger itself generates high temperatures via shock heating (Fig. 4), leading to a dynamical production of pions (see also [80]). Positively charged pions, π^+ , are largely absent in the inspiral, but are produced in small amounts in the post-merger, $Y_{\pi^+} \sim 3 \times 10^{-6}$, largely in regions of high temperature or at lower densities in the disk. On the other hand, most pions especially in very dense regions, $n \gg 2n_{\text{sat}}$ form a condensate, π_c , after merger. The presence of muons, μ , denoted by the split panel in Fig. 5, leads to a reduction in the pion condensate, consistent with muons being produced by pion-decay. This can be seen by overall local charge conservation, where the presence of muons leads to a necessary reduction in pions, as the baryon number (mainly constraining the protons) is always fixed.

We now analyze the muons, muon-type (anti)neutrinos, and electron type (anti)neutrinos (Figure 6). We can see that the muon fraction initially does not appreciably change from the initial value, $Y_\mu = 0.01$, we had fixed to a representative value [79]. During and after merger, Y_μ increases to between $Y_\mu \sim 0.027 - 0.045$ from higher muon chemical potentials in this hotter and denser environment. Note, this is similar to the results from [84], whose ‘5 neutrino species’ cases find significant muons only inside the high density remnant core.

In the middle row of Figure 6, we show the difference between Y_{ν_μ} and $Y_{\bar{\nu}_\mu}$. In the left panel, between both density contours, one sees a slight preference towards $\bar{\nu}_\mu$. With maximum values of $|Y_{\nu_\mu}| \lesssim 3 \times 10^{-3}$, these effects are minor enough to be dynamically unimportant. The surface of the stars features small amounts of $\bar{\nu}_\mu$, which

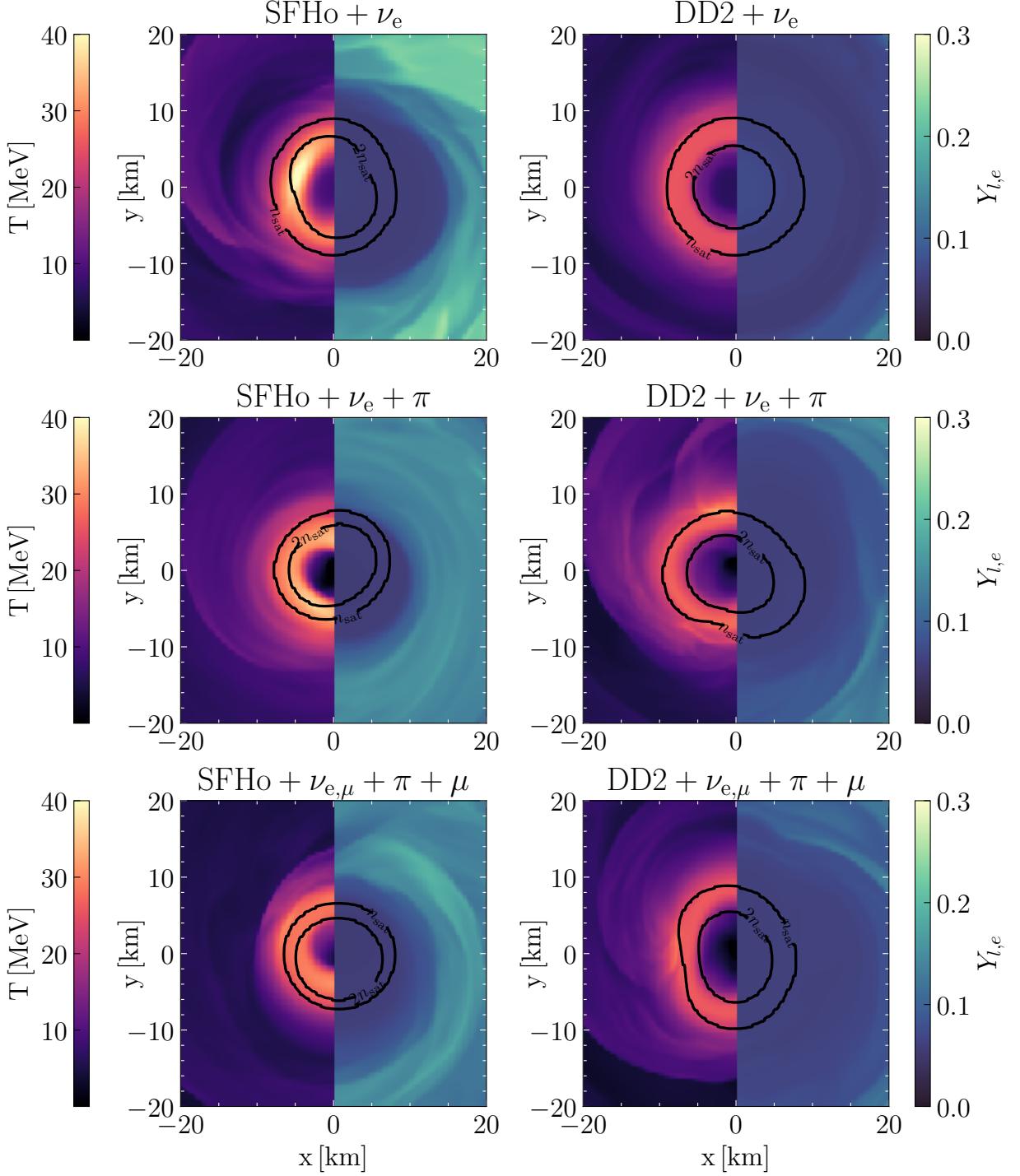


FIG. 4: Post-merger temperature, T , (left half) and electron lepton fractions, $Y_{l,e}$ (right half), taken ~ 20 ms after merger in the equatorial plane. Each panel corresponds to an EOS variant. Overlaid in black are the isodensity rest-mass contours at n_{sat} and $2n_{\text{sat}}$.

may, however, be contaminated by artificial heating at the surface, due to our numerical scheme not being well-balanced. In the middle row, middle column, we observe the production of Y_{ν_μ} at the hot merger interface. The

middle row, right column displays a much more prominent ‘anti neutrino ring’. This feature very closely tracks the high temperature ring in the remnant. Since the center of the remnant is relatively cooler (see Figure 4), the

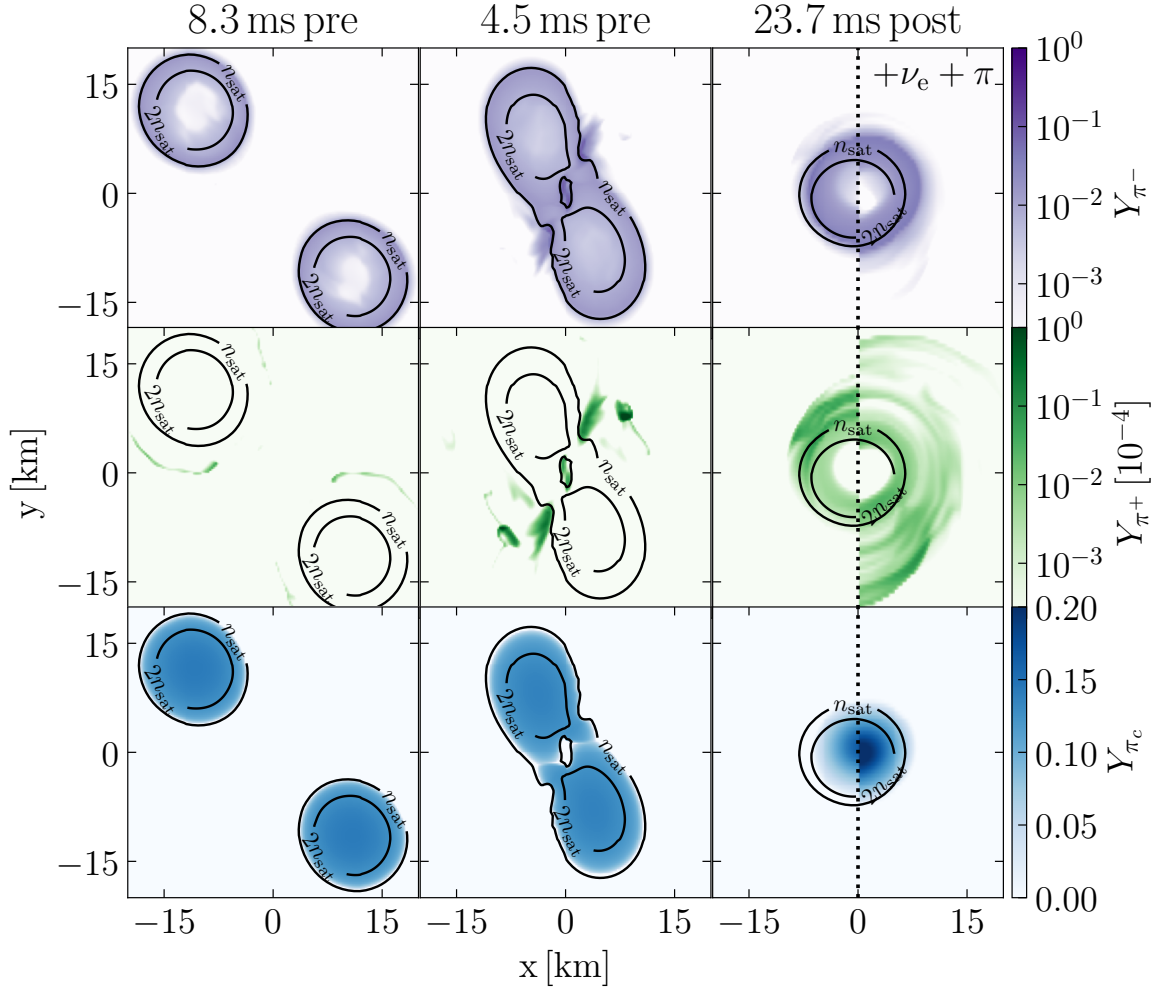


FIG. 5: Neutron star merger with trapped neutrinos, $\nu_{e,\mu}$, pions, π , and muons, μ , using the SFHo equation of state. (From left to right) Equatorial slices of particle fractions, Y_i , before merger, at contact, and during ringdown. (Top) Pion fraction of negatively charged thermal pions, π^- . (Middle) Pion fraction of positively charged thermal pions, π^+ (scaled by 10^4). (Bottom) Pion fraction for condensate, π_c . Black solid lines are the rest mass density contours at n_{sat} and $2n_{\text{sat}}$. In the last column, the left half of the panel includes muons whereas the right half of the column does not include muons. Notice the lighter shade in the condensate indicates the presence of muons (left) lowers the condensate fraction.

production of $\bar{\nu}_\mu$ is less prominent.

In the lower row of Figure 6, we show the difference between Y_{ν_e} and $Y_{\bar{\nu}_e}$. The nearly isolated neutron stars show negligible ν_e contributions. At contact, there is slight electron type neutrino production along the linear, diagonal, high temperature element. In the right column, we see higher ν_e concentrations in the center of the remnant. Note, for all three ν_e plots, the ν_e fractions track the μ^- fractions rather closely. This is a product of the muons decaying into $\bar{\nu}_e$ in Equation (2). Overall, our results are consistent with previous works [79, 92].

To better quantify the particle fractions in the rem-

nant, at ~ 20 ms after merger, we refer to Figure 7. Focus on the top panel of Figure 7. This displays Y_π as a function of number density n_b , normalized by n_{sat} , for the SFHo+ $\nu_{e,\mu}+\pi+\mu$ EOS. It is clear in the high density regime the presence of charged pions is greater, supporting our previous figures. Moreover, there is an inherent temperature-induced spread in the relation between n_b and Y_π . In particular, the shocked, higher temperature regime near the center of the remnant will exhibit multiple Y_π for a given n_b .

Instead of a monotonic increase of Y_π with n_b , there is nonmonotonicity $\sim 0.75n_{\text{sat}}$. Recall that the contri-

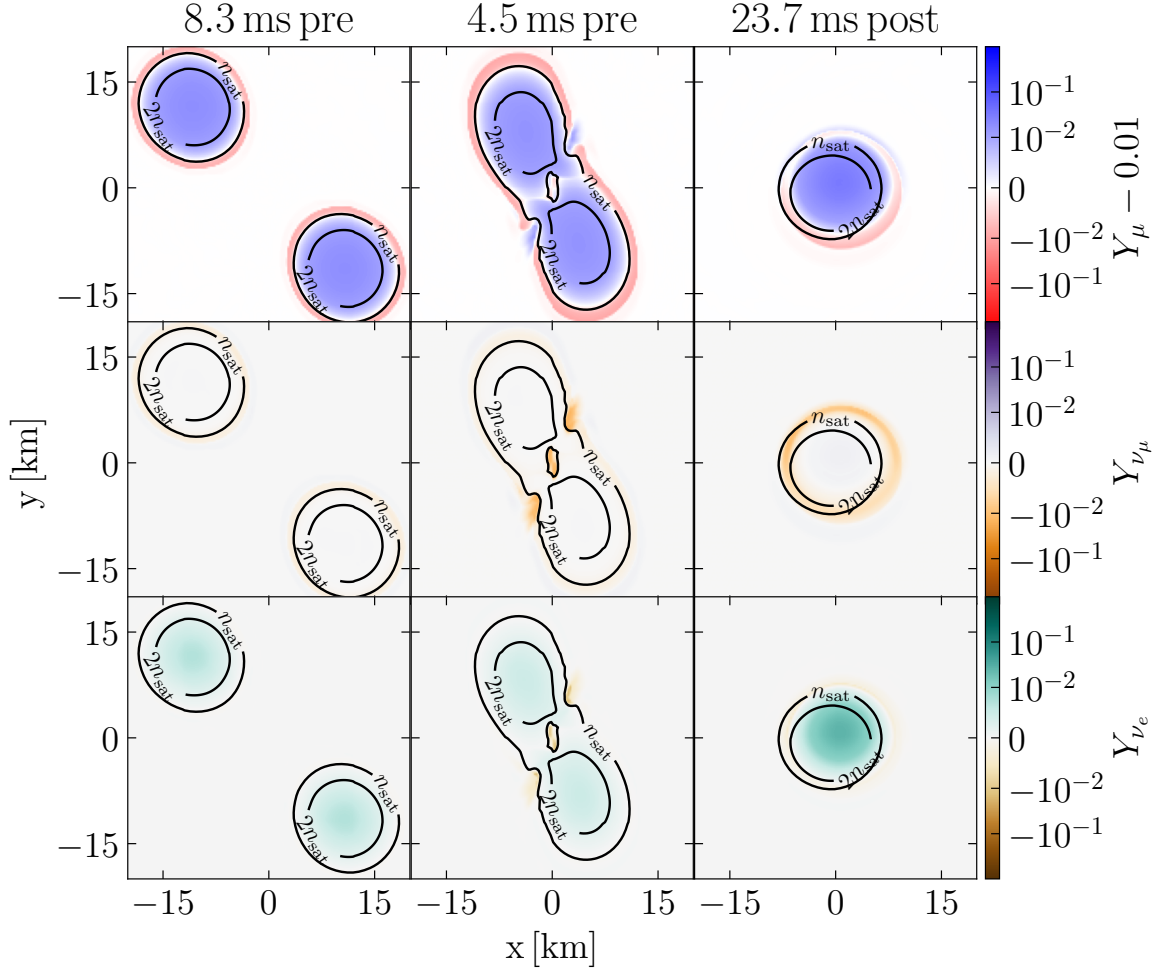


FIG. 6: Same as Figure 5 but for muon fraction, Y_μ , muon neutrino fraction Y_{ν_μ} , and electron neutrino fraction Y_{ν_e} . (Top) Muons are present in the cold isolated NSs and display an increased population in the remnant core as densities and temperatures increase. (Middle) Muon-type neutrino fraction. As the isolated NSs are constructed assuming zero temperature equilibrium, very few muon-type neutrinos are present. As temperatures increase at contact, an excess of $\bar{\nu}_\mu$ (negative Y_{ν_μ}) is apparent. (Bottom) Electron-type neutrino fraction, displaying high ν_e in the remnant core and higher $\bar{\nu}_e$ content in the high temperature ring.

Contributions from Y_π come from both condensate and thermal effects. When observing the plots for these species individually, we note a monotonic increase of condensate fraction with n_b . However, the thermal, charged pions exhibit the nonmonotonicity. This can be explained from the temperature profile within the remnant. As outlined in our methods, once a condensate begins to form (around $n_b/n_{\text{sat}} = 1$) the chemical potential of the thermally charged pions remains fixed at m_π . Referring to Equation (10), this implies $z = 1$. Thus, n_π will scale as $T^{3/2}$. Because of the presence of a high temperature ring around the remnant center (Figure 4), as one approaches the center, there will be nonmonotonic behavior in the

temperature as well.

In the middle panel of Figure 7, Y_μ as a function of n_b is shown. For low densities, the constant $Y_\mu = 0.01$ is displayed. However, at the density cutoff of $10^{14} \text{ g cm}^{-3}$, there is a decrease, followed by an increase at $\sim 0.45n_b$. The origin of this nonmonotonicity is different than the pion case. As detailed in Appendix A 1, at this density, we transition from the assumed $Y_\mu = 0.01$ to the parameterized $\tilde{Y}_{l,\mu}(\rho)$ in Equation (A3). Just above the density cutoff, $\tilde{Y}_{l,\mu}(\rho)$ admits $Y_\mu < 0.01$, resulting in the first decrease. At $n_b \sim 0.45n_{\text{sat}}$, $\tilde{Y}_{l,\mu}(\rho)$ allows higher values, resulting in a corresponding increase.

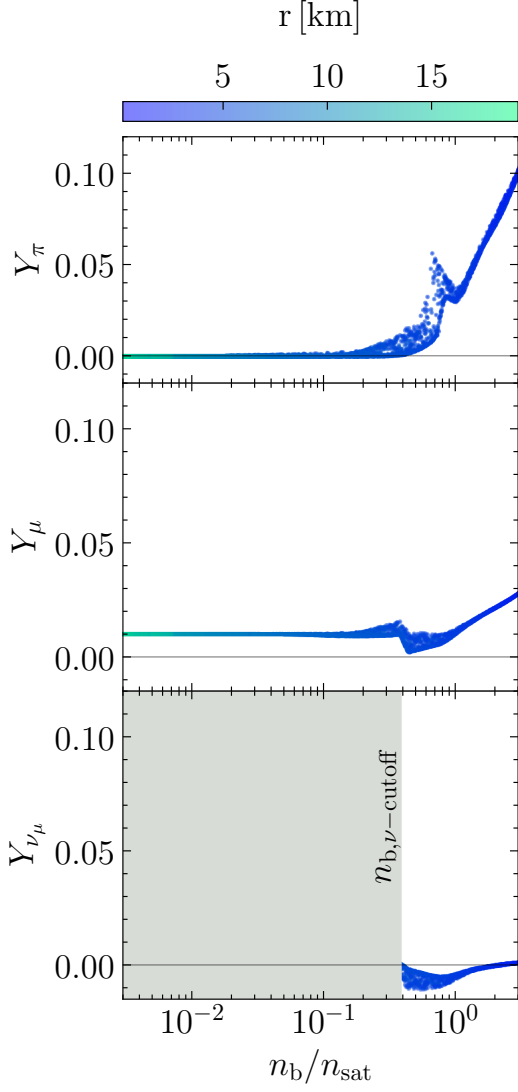


FIG. 7: Particle fractions, Y_i , as a function of normalized number density, n_b , in merger remnant for model SFHo+ $\pi + \mu + \nu_e \sim 20$ ms after merger. Colors indicate the radial distance, r , from the center.

The lower panel displays Y_{ν_μ} . Once one passes the density cutoff of $\rho \simeq 10^{14}$ g cm $^{-3}$, there is a minimum in Y_{ν_μ} occurring at a similar density regime to the non-monotonicity in Y_π . Recall Equation (12). Note, this scales with $T^3(F_2(\eta_\nu) - F_2(-\eta_\nu))$. At these densities, the temperature inversion is sufficient to prevent the Y_{ν_μ} from becoming more negative. When looking at the DD2 data, similar features in the particle fractions are present.

B. Quantifying Merger Dynamics

To begin describing the dynamics of the merger, we appeal to the temperature distribution as a function of n_b/n_{sat} in Figure 8. For all cases, we see increasing tem-

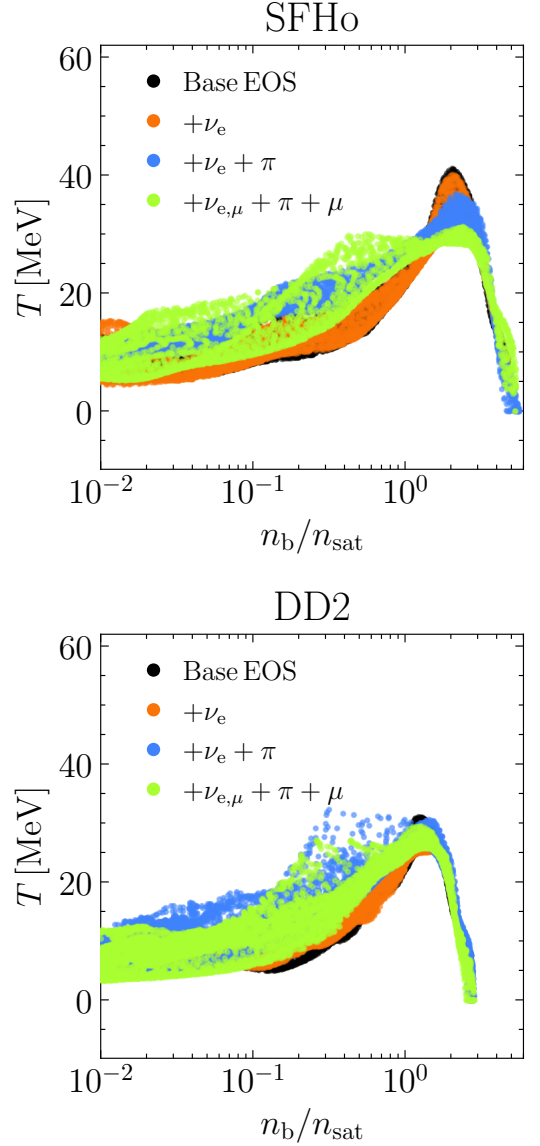


FIG. 8: Temperature, T , vs baryon number density, n_b , normalized by nuclear saturation density, n_{sat} , for the post merger remnant for two different base equations of state (DD2 and SFHo), modified by the particle contributions listed in the legend. The data is taken at ~ 20 ms after merger.

perature with increasing number density of the baryons, up until $\sim 2n_{\text{sat}}$. Beyond this density cut, the temperature decreases. This observation is consistent with the high temperature ring between n_{sat} and $2n_{\text{sat}}$, seen in Figure 4. For both the base EOS and $+\nu_e$ case, we see no major changes in the thermal distribution of the material, indicating ν_e has no major effect on the thermalization of the new remnant at low densities, when approximated as an ideal Fermi gas.

A more subtle feature occurs at the peak of the temperature distribution; we see a marginally smaller peak

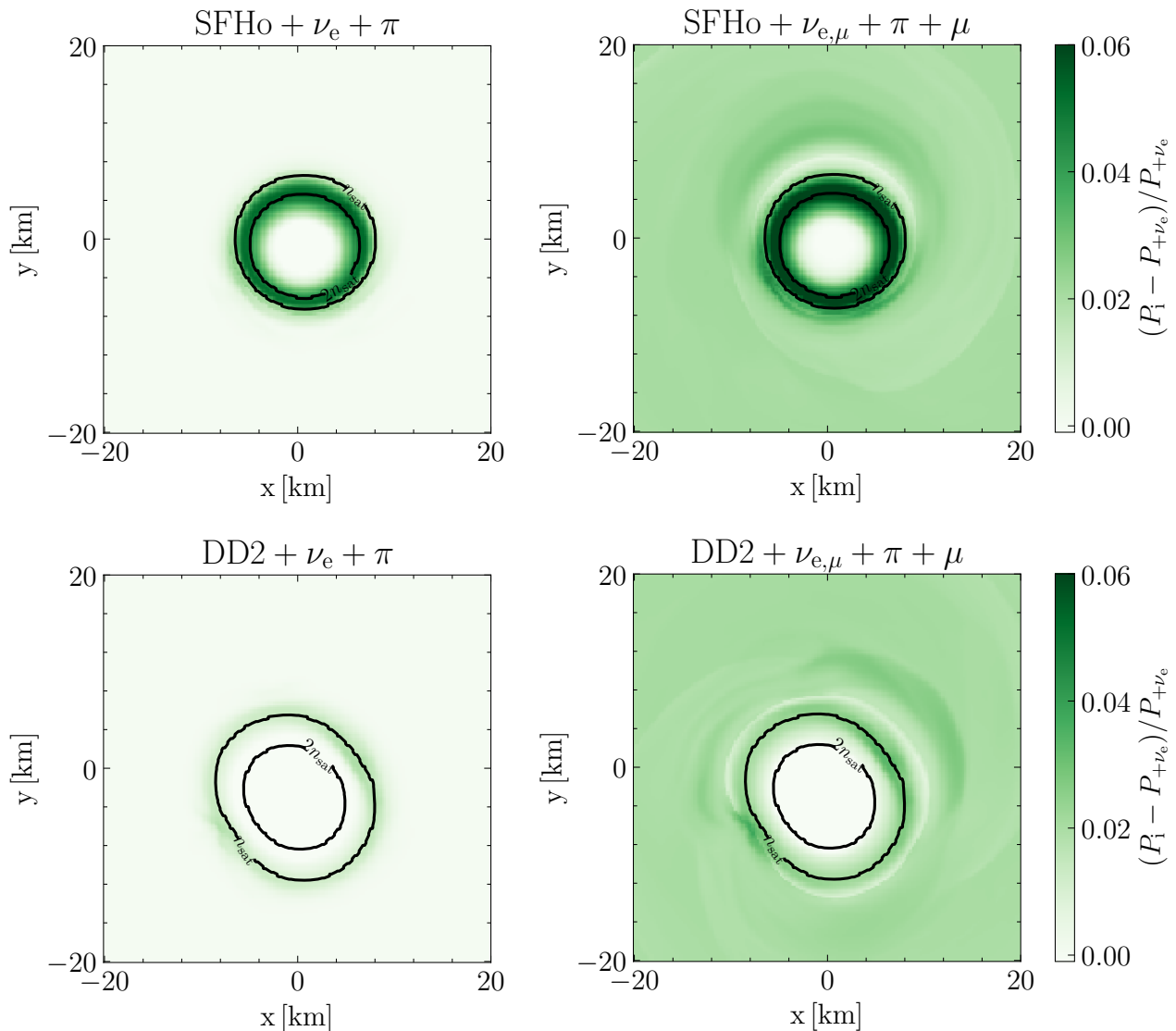


FIG. 9: Relative pressure difference as a result of different particle species. P_j denotes the pressure given a composition. Shown are results for two EOS (DD2 and SFHo) about ~ 20 ms after merger when comparing $+\nu_e + \pi$ vs $+\nu_e$ (Left) and $+\nu_{e,\mu} + \pi + \mu$ vs $+\nu_e$ (Right). Overplotted with black lines are the density contours for n_{sat} and $2n_{\text{sat}}$.

temperature in the $+\nu_e$ case. At contact between the no-longer isolated NS companions, there is a temperature spike that is of order 50 MeV. Combined with the high density material, this high temperature environment leads to a trapped (anti) neutrino population. Thus, the neutrinos provide a thermal energy sink for the merger.

For the $+\nu_e + \pi$ case, we see a similar increase in temperature as a function of n_b . Between $10^{-2}n_{\text{sat}}$ and n_{sat} , we see slightly higher temperature material at the $\sim 5\%$ level. Beyond $\sim 2n_{\text{sat}}$ the high temperature peak is lower, from ~ 40 MeV to ~ 35 MeV, compared to the $+\nu_e$ case. This lower peak is due to the thermal production of pions. This observation is supported by the top panel of Figure 7. Near n_{sat} , there is a local max-

imum that displays a nonmonotonicity in Y_π . This is directly sourced by the thermally charged pions, whereas the overall monotonic increase is sourced by the condensed pions. With a relatively greater population of new species in a high temperature regime, the energy can go into creating π rather than increasing the temperature of the baryons.

The $+\nu_{e,\mu} + \pi + \mu$ case shows similar behavior, with slightly larger spread in temperatures between $10^{-2}n_{\text{sat}}$ and n_{sat} . This may be due to the increased presence of muons. In particular, having an additional species present may allow for further particle production, acting as an additional sink for the thermal energy.

Focusing on the bottom panel of Figure 8 for DD2, we

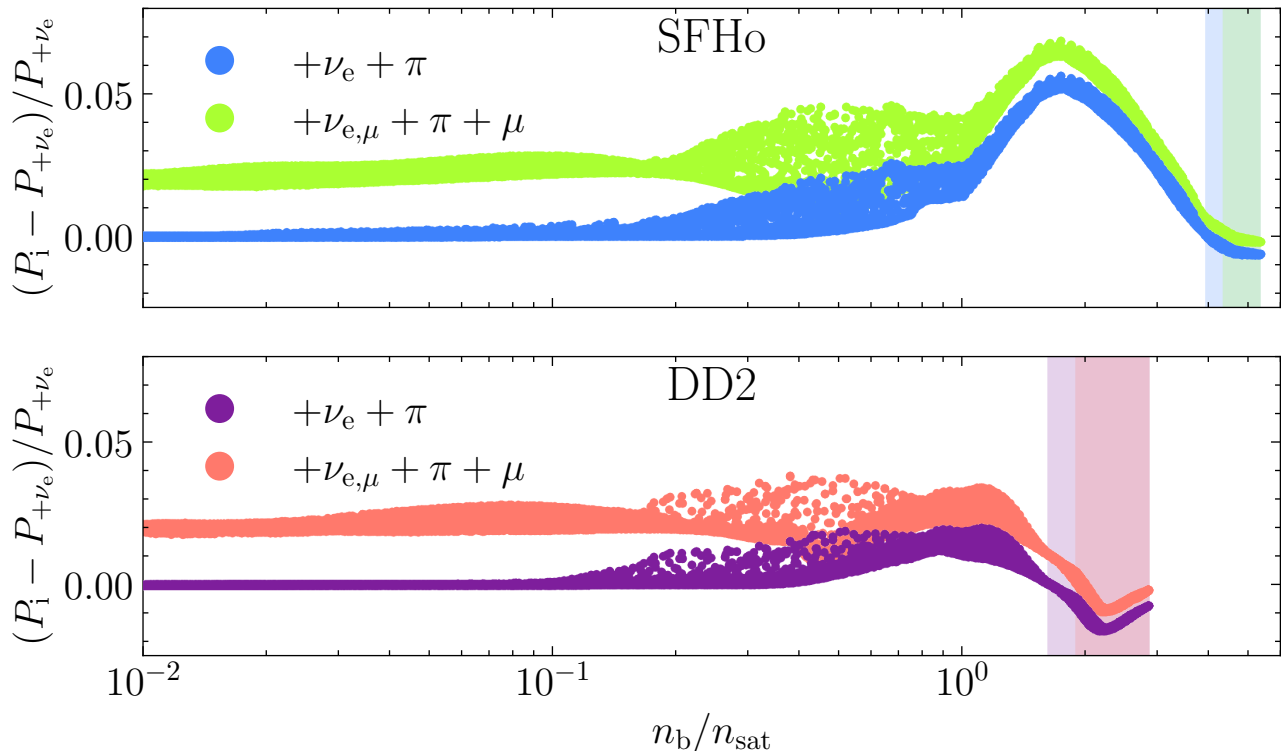


FIG. 10: Change in pressure in remnant for different SFHo EOSs (top) ~ 20 ms post merger and the DD2 EOSs (bottom). Each color represents the difference in pressure for the $+\nu_{e,\mu} + \pi + \mu$ and $+\nu_e + \pi$ compared against $+\nu_e$. Shaded regions indicate where pressures for the labeled EOS are lower than the $+\nu_e$ case.

see some qualitative similarities to SFHo. First, there is an increase in temperature vs n_b until $\sim n_{\text{sat}}$. Secondly, we do not see a major difference between unmodified DD2 and the ν_e case. Third, we see thermalization of the lower density material due to pions, albeit at a more extreme extent, compared to SFHo. This is illustrated by a more noticeable difference between the blue $+\nu_e + \pi$ points and the black DD2 points. This is counterbalanced with the inclusion of muons, leading to overall lower temperatures.

To better quantify what is driving the changes in the dynamics, we now analyze the contribution of different particle species via their pressure contributions. To this end, we perform a similar analysis previously done for the impact of neutrino-driven effects in the merger [72, 75]. Defining P_i as the pressure for an EOS with additional i -species, we compute $\Pi/P_{+\nu_e} = (P_i - P_{+\nu_e})/P_{+\nu_e}$ as the relative pressure difference to our fiducial model including trapped electron neutrinos [74]. The outcome is shown in Fig. 9. This figure is taken ~ 20 ms after merger for the $+\nu_{e,\mu} + \pi + \mu$ run for SFHo (top) and DD2 (bottom). It compares the pressures using the thermodynamic states found using the $+\nu_e$ run, with the $+\nu_e + \pi$, and $\nu_{e,\mu} + \pi + \mu$ cases. We note a max $\Pi/P_{+\nu_e}$ in the remnant in a ring ~ 7 km from the remnant center at the $\sim 6\%$ level. The left column compares $+\nu_e$

with $+\pi + \nu_e$ —essentially this comparison isolates the effects of the pions. While we see this region fitting nicely in between the n_{sat} and $2n_{\text{sat}}$ contours, it is in fact the temperature that is sourcing the pressure change. Figure 4 displays the temperature of the remnant. Physically, the temperature is sourcing the thermal population of pions, which provides support to the remnant. We see nice agreement between the temperature and pressure increases between Figure 4 and all panels of Figure 9.

In the right column of Figure 9, we compare $+\nu_{e,\mu} + \pi + \mu$ with the $+\nu_e$ case. This comparison isolates the effect of the pions and muons. We see similar behavior to the previous case, with pressure increases at the $\sim 6\%$ level in the high temperature ring surrounding the remnant center, still influenced by the thermal pions. However, when comparing the left column with the right column, one notices the effect of the muons and muon type (anti)neutrinos. Strikingly, there is a darker shade in the surrounding remnant material outside the contours at the $\sim 2\%$ level. This is a direct consequence of the trends seen in the middle row of Figure 7. The nonzero population of muons at lower density provide thermal support in the lower density material. When comparing the SFHo cases in the top row with the DD2 cases in the bottom row, we can see that the impact is more pronounced for

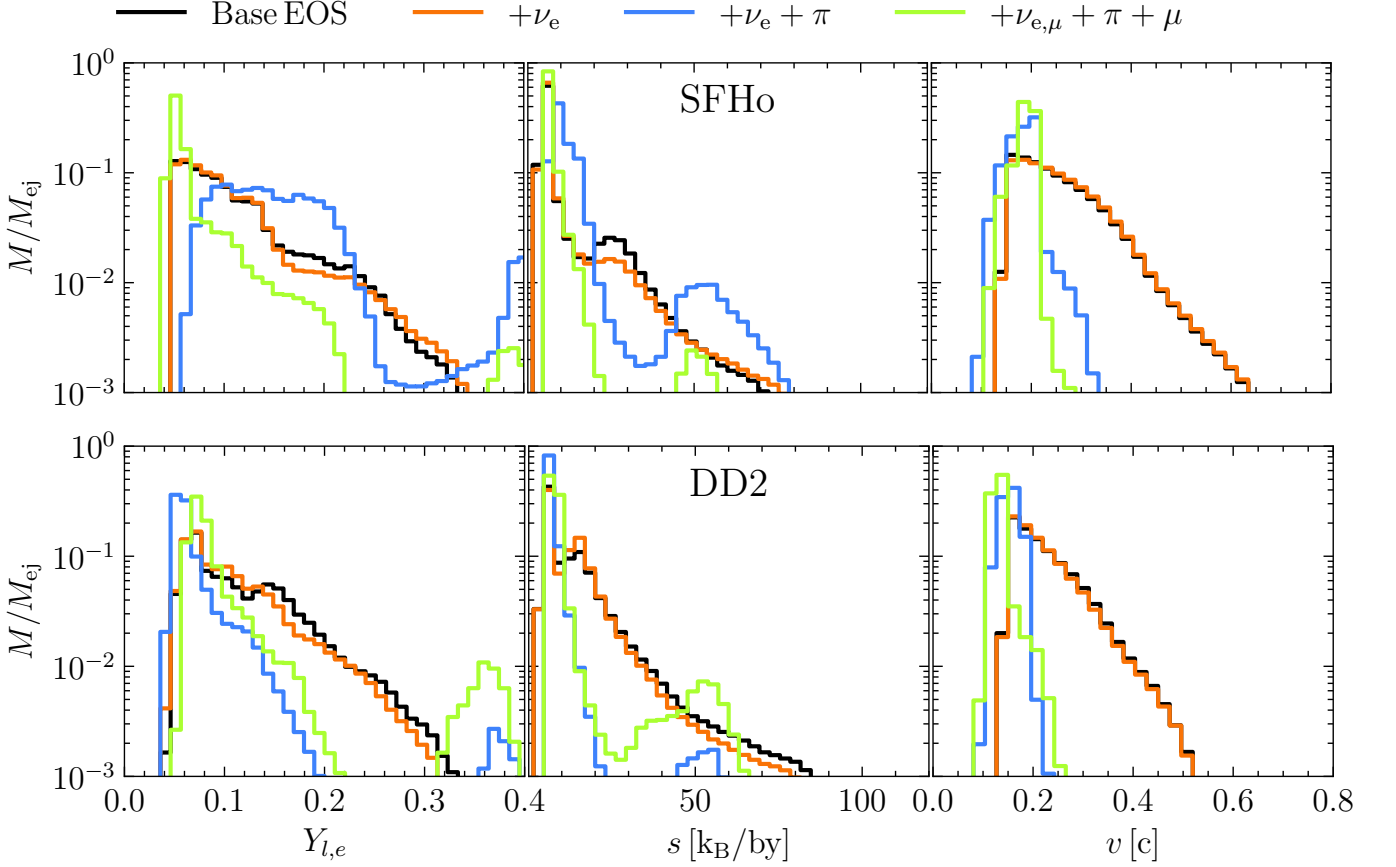


FIG. 11: Ejected mass fraction M relative to the total ejected mass M_{ej} for electron lepton number ($Y_{l,e}$), entropy per baryon (s), and velocity (v).

the SFHo EOS, due to the higher temperatures probed in the merger.

To better quantify these relations, Figure 10 displays $\Pi/P_{+\nu_e}$ as a function of n_b . We begin by examining the blue $+\nu_e + \pi$ points; these correspond to the data in the upper left panel of Figure 9. At low densities, we see $\Pi/P_{+\nu_e} \sim 0$, indicative of no pions at these lower densities $\lesssim 0.1n_b/n_{\text{sat}}$. This is supported by the middle panel of Figure 7, which also shows no charged pions in this density regime. At higher densities, this pressure increases to a maximum of $\sim 6\%$ at $n_b \sim 2n_{\text{sat}}$, followed by a sharp decrease to $\Pi \lesssim 0$. This increase corresponds to the n_b profile passing through the high temperature ring. As seen in Figure 4, at densities many times n_{sat} , the temperature drops at the center of the remnant. In this low temperature regime, the pion condensate dominates the pion production. Since the condensate does not contribute to pressure, one sees slightly negative $\Pi/P_{+\nu_e}$ at the highest densities, indicated by shaded regions.

The light green points in Figure 10 show $\Pi/P_{+\nu_e}$ for the $+\nu_{e,\mu} + \pi + \mu$ case. When comparing these light green points with the darker blue points, one can quantify the influence of muons on the NS merger dynamics. At $n_b \lesssim 0.1n_{\text{sat}}$, we note $\Pi/P_{+\nu_e} \sim 0.02$. As explained in

the right panel of Figure 9, this lower density material is supported by thermal contributions from muonic species. As n_b increases, we see a similar shape in the $\Pi/P_{+\nu_e}$ vs n_b curve to the $\nu_e + \pi$ case, systematically shifted by $\sim 2\%$. This behavior is expected. Observe the top row of Figure 1, focusing on the π_c blue, dashed line. When comparing the $+\nu_e + \pi$ case with the $+\nu_{e,\mu} + \pi + \mu$ cases, there is a decreased contribution from π_c . This decrease in π_c is due to the increased presence of charged muons. Lesser amounts of pion condensate paired with more muons contributes to a higher pressure support at $n_b \gtrsim 0.4n_{\text{sat}}$.

In the bottom panel, we see the same quantities for DD2. Both variants produce similar behavior at lower densities. However, the stiffer DD2 produces less pronounced $\Pi/P_{+\nu_e}$ beyond n_{sat} . Since the EOS is stiffer, it will settle to lower densities. Furthermore, the less compressible EOS does not produce temperatures as high during the collision, compared to SFHo. This combination of a less dense environment at lower temperatures is less conducive to creating muons and thermal pions. As such, the peak $\Pi/P_{+\nu_e}$ only reaches ~ 0.03 . With fewer pressure-providing pions and muons, compared to SFHo, the pion condensate allows a ΔP

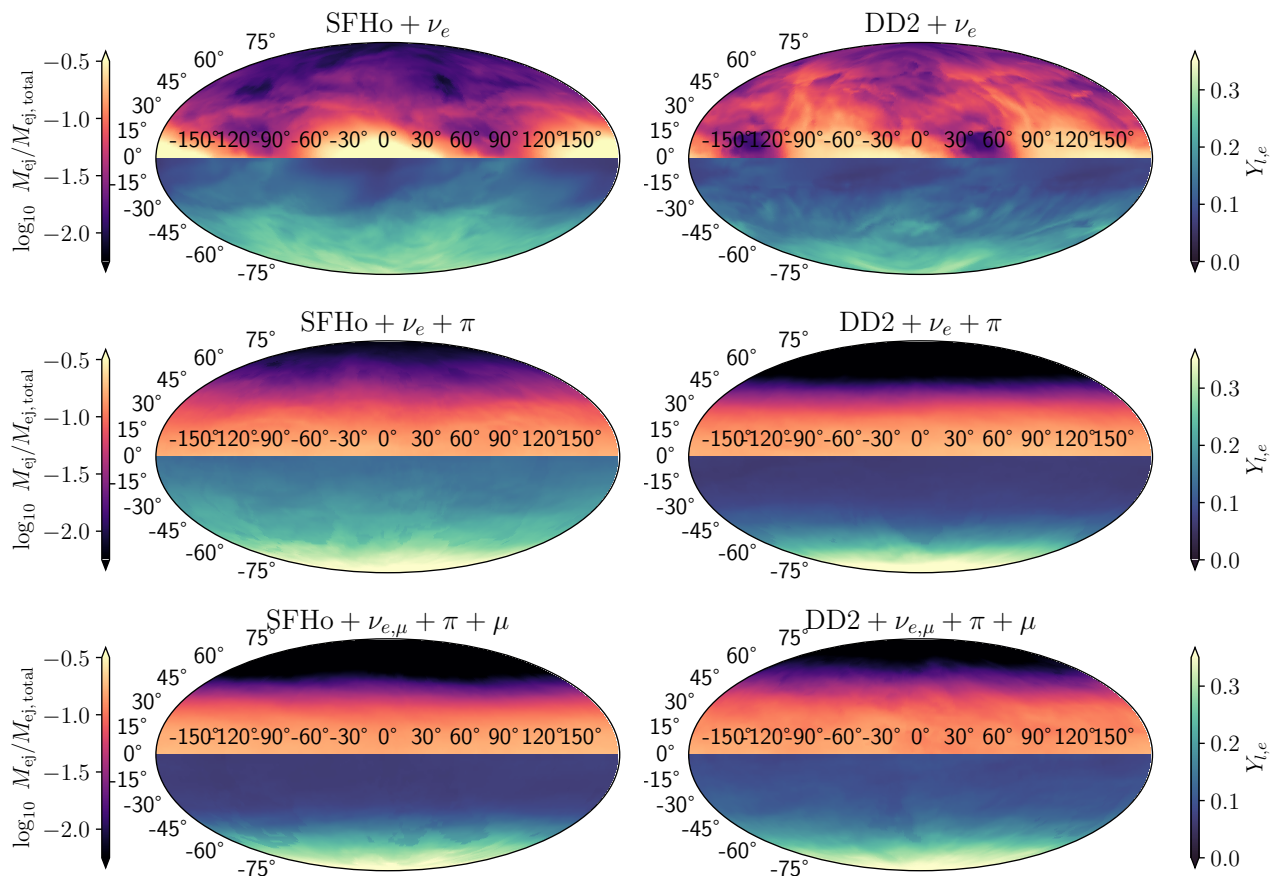


FIG. 12: In each panel, ejecta mass M_{ej} (top) and $Y_{l,e}$ distribution (bottom) for all 3 EOS variants. Brighter colors indicate more mass ejected and higher $Y_{l,e}$ along a particular direction. Generally, more matter, which is neutron rich (low $Y_{l,e}$) is ejected along the equator, leaving darker $Y_{l,e}$ colors along the equator.

	$M_{\text{ejecta}}^{\text{SFHo}} [M_{\odot}]$	$M_{\text{ejecta}}^{\text{DD2}} [M_{\odot}]$
Base EOS	7.00×10^{-4}	4.84×10^{-4}
$+\nu_e$	6.51×10^{-4}	4.90×10^{-4}
$+\nu_e + \pi$	6.20×10^{-3}	4.44×10^{-2}
$+\nu_{e,\mu} + \pi + \mu$	5.17×10^{-2}	1.44×10^{-2}

TABLE I: Ejecta masses for each simulation. Shown are the integrated unbound mass ejecta M_{ejecta} for each simulation. Different rows denote the added particle content to the base equations of state (EOS), DD2 and SFHo.

minimum of ~ -0.02 .

C. Mass Ejection

The potential kilonova afterglow of a NSNS event will crucially depend on the amount and composition of unbound mass ejected during merger [122]. We compute the ejected mass in our simulation by integrating the mass

flux,

$$\dot{M}_{\text{ej}} = \oint_{r=\text{const}} dS \sqrt{\gamma} \rho \frac{u^i}{u^0}, \quad (26)$$

over a sphere at radius, $r \sim 300$ km, for ~ 20 ms after the merger. We only include mass fluxes if the matter is unbound (i.e., can escape to infinity), according to $u_0 < -1$ (e.g., [123, 124]). In Table I, we report the values of the masses ejected for each simulation. The central column is mass ejecta values for SFHo ($M_{\text{ejecta}}^{\text{SFHo}}$) while the right column is for DD2 ($M_{\text{ejecta}}^{\text{DD2}}$). In line with [125], our control and $+\nu_e$ EOS cases give similar order of magnitude estimates for ejecta masses $\sim 10^{-4} M_{\odot}$.

To address the influence of different species for both EOSs, between the unmodified EOS and the $+\nu_e$ case, we do not see ejecta masses change more than ~ 7 percent. This narrow difference is consistent with similar behavior between the base EOS and $+\nu_e$ case seen in Figure 8. When comparing to the $+\nu_e + \pi$ cases, we note more mass by an order of magnitude. The majority of this mass is ejected after the initial tidal stream ejection. Due to pion condensate, the slightly more compact remnant seems to experience multiple bounces affecting the

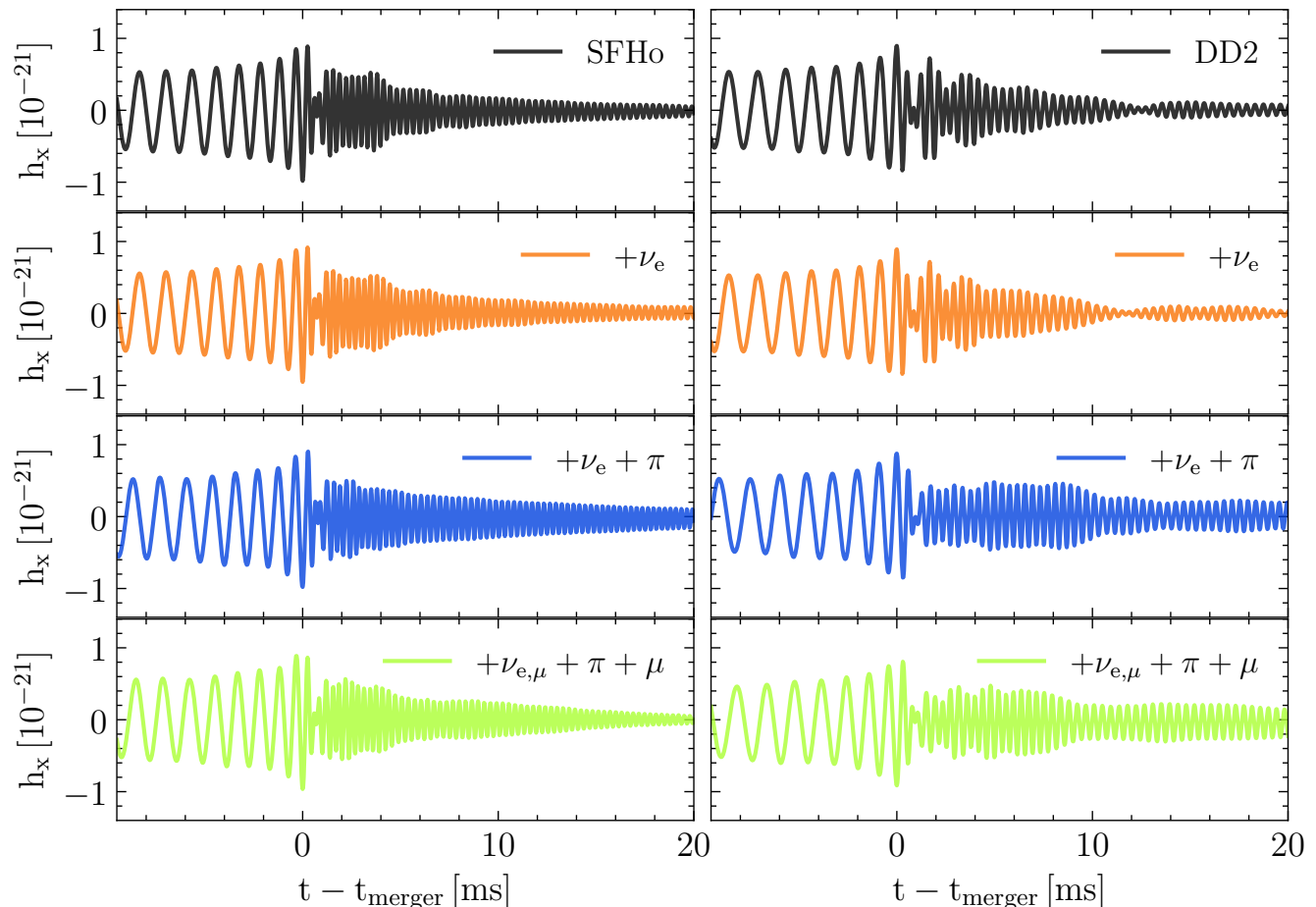


FIG. 13: Gravitational wave strain, h_x , for the different simulations extracted at a radius, $r \sim 1300$ km, with a detector distance of 30 Mpc. Columns denote the two different base equations of state, DD2 and SFHo. Rows indicate the added microphysical particle content. Times, t , are stated relative to the time of merger, t_{merger} .

production of fast ejecta [126]. Furthermore, this increase in mass can be linked to the more compact NS companions. As seen in the left panel of Figure 3, cold TOV stars will have pion condensate in their cores, creating more compact objects. This softening of the EOS likely will release more shock-heated ejecta. However, similar to [80], we note a larger than expected impact of pions on the ejecta mass, though the numbers we find may be subject to numerical resolution effects. We merely focus on the qualitative effect of each species shifting the ejecta mass to lower or higher values, depending on the EOS. Lastly, the influence of muons is nonlinear, whose effect depends on EOS, causing more ejecta for the softer SFHo and less ejecta for DD2.

We now address the distribution of material within ejecta, shown in Figure 11. The left column contains histograms of the $Y_{l,e}$ of the ejected material. The top row is for the SFHo EOS and the bottom row is for the DD2 EOS. For both unmodified EOSs, there is a peak in $Y_{l,e}$ at lower values ~ 0.075 , which is expected as the material is neutron rich. Similar to before, we notice little difference

in the ejecta between the unmodified EOS and $+\nu_e$ cases. We caution that this may be subject to assumptions in the neutrino treatment [73]. The $Y_{l,e}$ distribution is similar to other work that has examined $1.25 M_{\odot}$ equal mass mergers [125]. For both EOSs, we notice similar peaks in the $Y_{l,e}$ distributions when including pions and muons. Note, the higher $Y_{l,e} \geq 0.35$ content is lower in mass by nearly an order of magnitude, compared to the peak $Y_{l,e}$ ejecta, and sourced from NS atmosphere shed during the inspiral phase that is swept up by the tidal ejecta.

In the middle panels of Figure 11, we display the entropy per baryon of the ejecta (s). All distributions display a peak $s \sim 10 \text{ kb by}^{-1}$. For the unmodified EOS and $+\nu_e$ cases, both EOS show a gradual decline in the entropy profile. By contrast, the $+\nu_e + \pi$ and $+\nu_e, \mu + \pi + \mu$ cases show steep fall-offs in the s distribution. This material is sourced from ~ 5 ms after the initial tidal tail is launched. Since this material is not as actively shocked as the ejecta from initial contact, we expect lower entropies. The minor bump at $s \sim 50 \text{ kb by}^{-1}$ is from the initially shedded atmosphere.

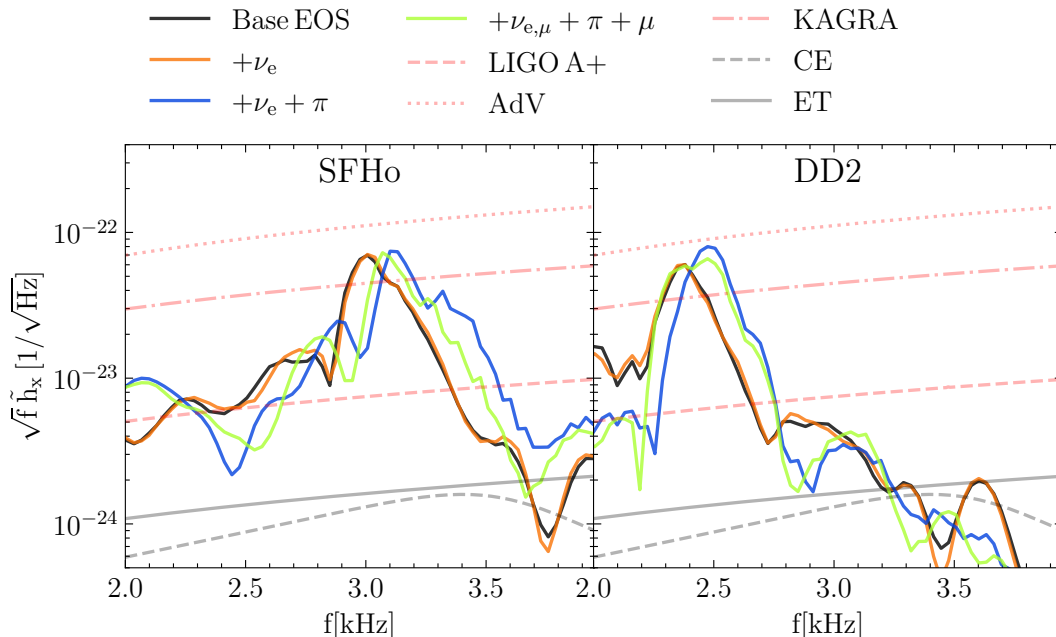


FIG. 14: Post-merger gravitational wave frequency spectrum at a distance of 30 Mpc. Shown is the effective strain, $\sqrt{f} \tilde{h}_x$, and the frequencies, f , probed in the merger. Different colors denote different particle contents, different columns vary the underlying equation of state model, either DD2 or SFHo. Overlaid are (expected) sensitivity curves for LIGO A+, Advanced Virgo (AdV), KAGRA, Cosmic Explorer (CE), and Einstein Telescope (ET).

In the right panel, we see the velocity distribution of the ejecta. For the similar base EOS and $+\nu_e$ cases, we note a distribution with velocity peak around $0.15 - 0.2c$. When compared to the cases that contain pions, we note a narrower velocity distribution, centered at a similar velocity peak. The source of this effect is from less initial shock heating in the NSNS remnant, see Figure 8. In these cases, the orbital energy that would have been deposited into the fluid kinetic energy is instead sourced into creating pions and muons. Moreover, similar to the entropy distribution, this ejecta is less shocked, leading to a slower moving secular drift. This slower ejecta is in line with the findings of Ref. [84].

Lastly, we investigate the spatial distribution of the ejecta, seen in Figure 12. Each column corresponds to a base EOS, SFHo (left) and DD2 (right). Each row corresponds to an EOS variant. The top hemisphere shows the log of the ejecta mass M_{ej} . The bottom hemisphere shows the mass-weighted average of $Y_{l,e}$. In the top row, both $+\nu_e$ variants exhibit mass ejection in the equatorial direction, indicated at latitudes $\lesssim 30^\circ$. In the lower hemisphere, the $Y_{l,e}$ distributions are moderately brighter along the poles, since most of the neutron rich ejecta sent along the equator lowers the mass-averaged $Y_{l,e}$.

In the middle row, the $+\nu_e + \pi$ variants appear more axisymmetric, indicated by relatively smooth distributions at all longitudes. As opposed to a single tidal tail that may exhibit asymmetries in the orbital plane,

the later time ejecta from the pions appears to diffuse equally along all azimuthal directions. The lower hemisphere shows a similar trend to the $+\nu_e$ cases, where the lower $Y_{l,e}$, neutron rich, material is ejected near the equator. During the inspiral, the artificial atmosphere that is ejected has a higher $Y_{l,e}$, compared to the non-pionic runs, contributing to the brighter pole regions. The bottom row $+\nu_{e,\mu} + \pi + \mu$ variants display similar distributions, compared to the $+\nu_e + \pi$ variants. Overall, the inclusion of pions seems to make the ejecta more axisymmetric.

D. Gravitational Wave Emission

Post-merger gravitational wave emission has been shown to correlate strongly with the underlying nuclear physics [40, 43–45, 127], especially if exotic degrees of freedom [51, 52, 56, 68, 69] and/or finite-temperature effects are accounted for [61–63]. Since the appearance of a trapped electron neutrino component inside the merger remnant alone may only cause small changes in the dynamics and gravitational wave emission [73–75], it is interesting to ask whether the systematic addition of π and μ change this picture. To this end we perform a systematic analysis and comparison of the gravitational wave emission of our simulations.

We begin by extracting the GW signal using the ψ_4 formalism [128, 129], and examining the time domain

waveform (TDWF) for the dominant $\ell = m = 2$ mode of the system in Figure 13. We can already see that there is overall good agreement in the inspiral and only small changes in the post-merger gravitational wave strain amplitude due to the addition of muons and pions. This is consistent with the expectation that most of the signal is governed by the cold equation of state, which is only marginally modified (see Sec. II G).

One of the main promising routes of obtaining additional information from the post-merger gravitational wave signal is via the dominant frequency peak of the gravitational wave strain [130–134]. In Fig. 14 we show the frequency spectrum of the post-merger gravitational wave strain, focusing mainly on the dominant frequency peak. We begin by comparing the impact of adding different microphysical correction to the equation of state. In line with previous works, we find that the adding of trapped electron neutrinos does not appreciable alter the gravitational wave emission [73, 75, 98], although current simulations are likely not in a convergent regime [74, 75]. We investigate the impact of adding π to the EOS. We already found earlier that pions lead to a net softening (more compact neutron stars) of the equation of state, which generically should translate to higher frequencies. In line with this expectation, we find that for both EOS adding pions causes a shift of around 100 Hz of the post-merger gravitational wave signal, although the impact on SFHo seems slightly more pronounced. Such difference is consistent with uncertainties of quasi-universal relations [47, 49]. Finally, we also investigate the impact of μ , and trapped ν_μ . Similar to the addition of trapped ν_e , we find that the impact on the post-merger gravitational wave signal is small, though we caution that μ can in principle regulate the population of π , as seen in the amount of pion condensation (Fig. 5). While these frequencies are out of the current frequency sensitivity bands for the LIGO-Virgo-KAGRA detectors [135], these calculations stress the importance of capturing proper microphysics for accurate predictions of future NSNS waveforms to optimize future high frequency GW detectors.

IV. CONCLUSIONS

In this work, we have investigated the impact of trapped electron and muon neutrinos, muons and pions on the post-merger phase of a neutron star coalescence. Assuming that neutrinos are trapped and that the muons and pion decay are in equilibrium, we have constructed several equations of state systematically varying the microphysics content. We have then performed fully general-relativistic neutron star merger simulations to study the impact of these equations of state on the mass ejection and gravitational wave emission. Our results also present a detailed investigation into the regions of the remnant most sensitive to pion condensation. Our main findings are consistent with previous works [79, 80, 84], and can be summarized as follows:

Pions have a measurable impact on the temperature distribution of matter in the remnant from $\sim 0.01n_{\text{sat}} - n_{\text{sat}}$. When present with pions, the inclusion of muons limits the amount of pion condensate formed in the merger remnant (Figs. 1 and 2). For matter in the core of the remnant, because $\mu_n - \mu_p$ is limited by the pion mass, ν_e and $\bar{\nu}_e$ production will be limited. In the presence of muons, thermal pions provide pressure support in the high temperature ring around the remnant center, while the muons provide pressure support in the lower density material, Figure 9 and Figure 10. For softer EOSs, in the presence of muons, the peak GW frequency can shift higher by $\sim 5\%$. For stiffer EOSs, this peak only changes marginally, Figure 14. Overall, the frequency shifts in the post-merger gravitational wave spectrum are of comparable order to those of finite-temperature [63, 65] and weak-interaction effects [74, 75].

Although our results are part of a first number of steps towards a consistent inclusion of muon and muon neutrinos into neutron star merger simulations, they need to be improved in several ways. First, neutrinos should be modelled using fully consistent radiation transport schemes [136–138]. This is particularly important in correctly tracking the muonic lepton fraction, which we have crudely approximated here. Furthermore, we treat π as ideal Bose-Einstein gasses, while treating μ as ideal Fermi gasses. To be more consistent, modeling the transport of these charged particles would be ideal. We also neglect the density dependence of the pion mass. Similar to [80], we use the vacuum mass to present optimistic estimates, to see if these effects are observable under ideal conditions.

For future work, we plan to also extend beyond the NSNS system and better quantify the influence of these particles in the core-collapse supernova context [81]. Furthermore, how $\pi + \mu$ may couple with more exotic particles like axions remains an interesting route to pursue [139, 140].

ACKNOWLEDGMENTS

The authors are grateful for helpful conversations with Eleonora Loffredo, Ninoy Rahman, and Javier Roulet. Analysis for this work was done using `matplotlib` [141], `numpy` [142], `scipy` [143] and `kuibit` [144]. M.A.P. was supported by the Sherman Fairchild Foundation, NSF grant PHY-2309211, PHY-2309231, and OAC-2209656 at Caltech. ERM acknowledges supported by the National Science Foundation under grants No. PHY-2309210 and OAC-2103680. This work mainly used Delta at the National Center for Supercomputing Applications (NCSA) through allocation PHY210074 from the Advanced Cyberinfrastructure Coordination Ecosystem: Services & Support (ACCESS) program, which is supported by National Science Foundation grants #2138259, #2138286, #2138307, #2137603, and #2138296. Additional simulations were performed on the NSF Frontera supercomputer under grant AST21006.

Appendix A: Repopulating the Equation of State with New Species

1. The Choice of Muonic Lepton Fraction $Y_{l,\mu}$

The choice of $Y_{l,\mu}$ requires some care. Informed by the results of [79], the muonic lepton fraction at densities below 10^{14} g cm $^{-3}$ has been shown to be trapped at small values. Following Appendix A in [80]—and similar to the value used in [79]—we fix $Y_{l,\mu} = 0.01$, which has been shown to replicate muon lepton fractions in merger simulations.

Above the density cut of 10^{14} g cm $^{-3}$, the NS matter has been shown to trap the local muonic particle fractions of the cold, isolated NS companions before merger [79]. Hence, our goal is to construct an expression of muonic lepton fraction as a function of density $\tilde{Y}_{l,\mu}(\rho)$. Begin by assuming cold, neutrinoless β equilibrium. By cold, we select a temperature of 0.1 MeV that is near the bottom of the EOS tables. Equation (4) provides two expressions for β equilibrium and its relation to the muonic chemical potential:

$$\mu_e(\rho, T_{\text{low}}, Y_p) = \mu_n(\rho, T_{\text{low}}, Y_p) - \mu_p(\rho, T_{\text{low}}, Y_p), \quad (\text{A1})$$

$$\mu_\mu(\rho, T_{\text{low}}, Y_p) = \mu_e(\rho, T_{\text{low}}, Y_p). \quad (\text{A2})$$

To construct $\tilde{Y}_{l,\mu}(\rho)$ using this two equation system, we use an iterative procedure.

1. At a given ρ , begin with a trial guess \hat{Y}_p .
2. From the old EOS, use $(\rho, T_{\text{low}}, \hat{Y}_p)$ to find $\mu_e(\rho, T_{\text{low}}, \hat{Y}_p)$.
3. Using Equation (8), T_{low} , and μ_e , calculate n_{e^\pm} .
4. Convert to $Y_e = (n_{e^-} - n_{e^+})/(\rho/m_{\text{baryon}})$.
5. Using Equation (A2), equate $\mu_\mu = \mu_e(\rho, T_{\text{low}}, \hat{Y}_p)$.
6. Using Equation (8), T_{low} , and μ_μ , calculate n_{μ^\pm} .
7. Convert to $Y_\mu = (n_{\mu^-} - n_{\mu^+})/(\rho/m_{\text{baryon}})$.
8. Using Equation (5), update $\hat{Y}_p = Y_e + Y_\mu$.
9. If \hat{Y}_p does not converge, return to step 2. If \hat{Y}_p converges, record Y_μ , move to the next ρ , and return to step 1.

Condensing our assumptions regarding the muons

$$Y_{l,\mu}(\rho) = \begin{cases} \tilde{Y}_{l,\mu}(\rho), & \text{if } \rho \geq 10^{14} \text{ g cm}^{-3} \\ 0.01, & \text{if } \rho < 10^{14} \text{ g cm}^{-3}. \end{cases} \quad (\text{A3})$$

2. No Pion Condensate

At each entry of $\text{EOS}_{\text{old}}(\rho, T, Y_p)$, baryon chemical potentials $(\mu_n - \mu_p)$ are provided. If $(\mu_n - \mu_p) < m_\pi^-$, a pion condensate will not form. The unmodified EOS table provides thermodynamic quantities in terms of charge fraction $\text{EOS}_{\text{old}}(\rho, T, Y_p)$. We retabulate in terms of lepton fraction of electrons, $Y_{l,e}$; thus the first term on the right-hand side of Equation (18) is fixed at a given thermodynamic entry $(\rho, T, Y_{l,e})$. At a given $\rho, T, Y_{l,e}$ begin with a guess of $\hat{Y}_p = Y_{l,e}$; calculate μ_n, μ_p , and μ_e from $\text{EOS}_{\text{old}}(\rho, T, \hat{Y}_p)$. Noting chemical equilibrium,

$$\mu_{\nu_e} = \mu_e(\rho, T, \hat{Y}_p) - \mu_n(\rho, T, \hat{Y}_p) + \mu_p(\rho, T, \hat{Y}_p). \quad (\text{A4})$$

We calculate the $(Y_{\nu_e}(\mu_{\nu_e}, \rho, T) - Y_{\bar{\nu}_e}(\mu_{\nu_e}, \rho, T))$ terms using Equation (12). With a known ρ , use Equation (A3) to calculate $Y_{l,\mu}$.

To calculate the $(Y_{\nu_\mu} - Y_{\bar{\nu}_\mu})$ terms, we remind ourselves of Equation (17), with explicit dependencies

$$Y_{l,\mu} = Y_\mu(\hat{\mu}_\mu, \rho, T) + Y_{\nu_\mu}(\hat{\mu}_{\nu_\mu}, \rho, T) - Y_{\bar{\nu}_\mu}(-\hat{\mu}_{\nu_\mu}, \rho, T). \quad (\text{A5})$$

In Equation (A5), $Y_{l,\mu}$ is fixed according to Equation (A3). Using Equation (4), $\hat{\mu}_{\nu_\mu}$ can be written as

$$\hat{\mu}_\mu = \mu_n(\rho, T, \hat{Y}_p) - \mu_p(\rho, T, \hat{Y}_p) + \hat{\mu}_{\nu_\mu}. \quad (\text{A6})$$

Applying Equation (8) and Equation (12) to Equation (A5), one can solve for $\hat{\mu}_{\nu_\mu}$ numerically, as $\hat{\mu}_{\nu_\mu}$ is the only unknown in the equation. Using the newly found $\hat{\mu}_{\nu_\mu}$, Equation (12) gives the needed $Y_{\nu_\mu} - Y_{\bar{\nu}_\mu}$ in Equation (18).

For Y_π , note Equation (5) to obtain $\mu_\pi = \mu_n(\rho, T, \hat{Y}_p) - \mu_p(\rho, T, \hat{Y}_p)$. Apply Equation (10) to yield Y_π . Adding together all particle fractions gives a new \hat{Y}_p . Return to the beginning of the procedure to repeat until convergence. Once a converged $Y_{p,\text{new}}$ is obtained, move to the next $(\rho, T, Y_{l,e})$ entry and repeat.

3. Pion Condensate

In certain thermodynamic settings, $(\mu_n - \mu_p) > m_\pi^-$, a pion condensate can form in the NS remnant. In this case, the procedure to calculate Y_p changes. Begin with $(\rho, T, Y_{l,e})$. Select a trial $\hat{Y}_p = Y_{l,e}$. Repeat the procedure in Section A2 until convergence, giving a temporary $Y_{p,\text{temp}}$. If $\text{EOS}_{\text{old}}(\rho, T, Y_{p,\text{temp}})$ produces $(\mu_n - \mu_p) > m_\pi^-$, a condensate will be produced. In this case, as in Section II of [80], begin by iterating over EOS_{old} to find Y_p for

$$\mu_n(\rho, T, \hat{Y}_p) - \mu_p(\rho, T, \hat{Y}_p) = m_\pi^-, \quad (\text{A7})$$

the maximum chemical potential for pions. With Y_p in hand, observe the governing charge neutrality condition

when condensate is present

$$Y_{\pi}^{\text{cold}} = Y_p - Y_e - Y_{\mu} - Y_{\pi}^{\text{thermal}}. \quad (\text{A8})$$

Expanding with the definition of lepton fractions gives,

$$Y_{\pi}^{\text{cold}} = Y_p - Y_{l,e} + (Y_{\nu_e} - Y_{\bar{\nu}_e}) + Y_{l,\mu} + (Y_{\nu_{\mu}} - Y_{\bar{\nu}_{\mu}}) + Y_{\pi}^{\text{thermal}}. \quad (\text{A9})$$

As before, $Y_{l,e}$ is the known EOS entry. With a known (ρ, T, Y_p) one calculates μ_n, μ_p , and μ_e , and, using Equation (4), calculates μ_{ν_e} . Applying Equation (12) gives $Y_{\nu_e} - Y_{\bar{\nu}_e}$. As density is known, $Y_{l,\mu}$ is given by Equation (A3). As before, a similar iterative procedure is followed to solve Equation (A5) when $\mu_{\mu} = \mu_{\nu_{\mu}} + m_{\pi^-}$, giving $Y_{\nu_{\mu}} - Y_{\bar{\nu}_{\mu}}$. Lastly, Y_{π}^{thermal} is calculated using Equation (10) for $\mu_{\pi^{\pm}} = \mp m_{\pi^-}$. Any remaining charge after evaluating Equation (A9) represents the charge fraction of the condensate. In certain rare cases near the edge of the EOS table, and at temperatures beyond realistic simulation temperatures $\gtrsim 100$ MeV, the right-hand side of Equation (A9) can produce a negative number. In these cases, we floor the value of $Y_{\pi}^c = 0$.

While in certain proton rich conditions μ_{π^+} can exceed the charged pion mass, we do not expect these conditions in NSNS mergers [80], so we do not account for the effect of positively charged pion condensate.

4. Retabulating the EOS

At this point, the chemical potentials and particle fractions have been calculated for the new species. With these updated species, the charge, or proton, fraction has

now changed. Our original EOS is tabulated according to rest mass density, temperature, and proton (charge) fraction Y_p as (ρ, T, Y_p) . With the addition of pions and muons, this brings the total number of charge carriers to four: protons, electrons/positrons, muons, and pions. In principle, this means thermodynamic quantities are uniquely determined by a six dimensional parameter space $(\rho, T, Y_p, Y_e, Y_{\mu}, Y_{\pi})$. Similar to the unmodified EOS, charge neutrality in Equation (5) brings it down to five dimensions $(\rho, T, Y_p, Y_{\mu}, Y_{\pi})$. Assuming a known prescription for $Y_{l,\mu}$ brings the unique degrees of freedom to (ρ, T, Y_p, Y_{π}) and assuming chemical equilibrium through Equation (4) reduces the set to three thermodynamic dimensions (ρ, T, Y_p) .

In our simulations, one of our assumptions is that the lepton number is advected along with the fluid, consistent with [79]. Thus, to match the EOS calls within FILL, we must now retabulate the EOS according to $Y_{l,e}$ instead of Y_p ; essentially an EOS call will go from $\text{EOS}_{\text{old}}(\rho, T, Y_{p,\text{old}} = Y_e)$ to $\text{EOS}_{\text{new}}(\rho, T, Y_{l,e})$. In words, the third thermodynamic index now will represent $Y_{l,e}$, not Y_p . Originally, quantities like the sound speed, baryon chemical potentials, and pressure were uniquely determined by $(\rho, T, Y_{p,\text{old}} = Y_e)$. However, with the updated charge fraction, we loop through thermodynamic space $(\rho, T, Y_{l,e})$, remembering every entry has a corresponding $Y_{p,\text{new}}$. For every $(\rho, T, Y_{l,e})$ entry, set $\text{EOS}_{\text{new}}(\rho, T, Y_{l,e}) = \text{EOS}_{\text{old}}(\rho, T, Y_{p,\text{new}})$. This equation signifies updating already existing quantities like the sound speed, baryon chemical potentials, and pressure to be consistent with the new proton fractions. As a second step, we must add contributions to the pressure and specific internal energy, now that new particle species are present. This returns the discussion to Section IID.

-
- [1] J. M. Lattimer and M. Prakash, *Phys. Rept.* **442**, 109 (2007), [arXiv:astro-ph/0612440](#).
 - [2] J. M. Lattimer and M. Prakash, *Phys. Rept.* **621**, 127 (2016), [arXiv:1512.07820 \[astro-ph.SR\]](#).
 - [3] M. Oertel, M. Hempel, T. Klähn, and S. Typel, *Rev. Mod. Phys.* **89**, 015007 (2017), [arXiv:1610.03361 \[astro-ph.HE\]](#).
 - [4] R. Kumar et al. (MUSES), *Living Rev. Rel.* **27**, 3 (2024), [arXiv:2303.17021 \[nucl-th\]](#).
 - [5] F. Özel and P. Freire, *Ann. Rev. Astron. Astrophys.* **54**, 401 (2016), [arXiv:1603.02698 \[astro-ph.HE\]](#).
 - [6] J. Schaffner and I. N. Mishustin, *Phys. Rev. C* **53**, 1416 (1996), [arXiv:nucl-th/9506011](#).
 - [7] L. Tolos and L. Fabbietti, *Prog. Part. Nucl. Phys.* **112**, 103770 (2020), [arXiv:2002.09223 \[nucl-ex\]](#).
 - [8] F. Weber, *Prog. Part. Nucl. Phys.* **54**, 193 (2005), [arXiv:astro-ph/0407155](#).
 - [9] E. Annala, T. Gorda, A. Kurkela, J. Nättilä, and A. Vuorinen, *Nature Phys.* **16**, 907 (2020), [arXiv:1903.09121 \[astro-ph.HE\]](#).
 - [10] G. Baym and E. Flowers, *Nucl. Phys. A* **222**, 29 (1974).
 - [11] P. Haensel and M. Proszynski, *Astrophys. J.* **258**, 306 (1982).
 - [12] B. B. Brandt, G. Endrodi, E. S. Fraga, M. Hippert, J. Schaffner-Bielich, and S. Schmalzbauer, *Phys. Rev. D* **98**, 094510 (2018), [arXiv:1802.06685 \[hep-ph\]](#).
 - [13] A. L. Watts et al., *Rev. Mod. Phys.* **88**, 021001 (2016), [arXiv:1602.01081 \[astro-ph.HE\]](#).
 - [14] G. Raaijmakers et al., *Astrophys. J. Lett.* **893**, L21 (2020), [arXiv:1912.11031 \[astro-ph.HE\]](#).
 - [15] S. Bogdanov et al., *Astrophys. J. Lett.* **914**, L15 (2021), [arXiv:2104.06928 \[astro-ph.HE\]](#).
 - [16] M. C. Miller et al., *Astrophys. J. Lett.* **918**, L28 (2021), [arXiv:2105.06979 \[astro-ph.HE\]](#).
 - [17] S. Vinciguerra et al., *Astrophys. J.* **961**, 62 (2024), [arXiv:2308.09469 \[astro-ph.HE\]](#).
 - [18] N. Rutherford et al., *Astrophys. J. Lett.* **971**, L19 (2024), [arXiv:2407.06790 \[astro-ph.HE\]](#).
 - [19] C. Drischler, J. W. Holt, and C. Wellenhofer, *Ann. Rev. Nucl. Part. Sci.* **71**, 403 (2021), [arXiv:2101.01709 \[nucl-th\]](#).
 - [20] B. P. Abbott et al. (LIGO Scientific, Virgo), *Phys. Rev. Lett.* **119**, 161101 (2017), [arXiv:1710.05832 \[gr-qc\]](#).
 - [21] B. P. Abbott et al. (LIGO Scientific, Virgo), *Astrophys.*

- J. Lett. **892**, L3 (2020), arXiv:2001.01761 [astro-ph.HE].
- [22] L. Baiotti, *Prog. Part. Nucl. Phys.* **109**, 103714 (2019), arXiv:1907.08534 [astro-ph.HE].
- [23] C. Cutler and E. E. Flanagan, *Phys. Rev. D* **49**, 2658 (1994), arXiv:gr-qc/9402014.
- [24] E. E. Flanagan and T. Hinderer, *Phys. Rev. D* **77**, 021502 (2008), arXiv:0709.1915 [astro-ph].
- [25] K. Chatziioannou, C.-J. Haster, and A. Zimmerman, *Phys. Rev. D* **97**, 104036 (2018), arXiv:1804.03221 [gr-qc].
- [26] C. Raithel, F. Özel, and D. Psaltis, *Astrophys. J. Lett.* **857**, L23 (2018), arXiv:1803.07687 [astro-ph.HE].
- [27] E. Annala, T. Gorda, A. Kurkela, and A. Vuorinen, *Phys. Rev. Lett.* **120**, 172703 (2018), arXiv:1711.02644 [astro-ph.HE].
- [28] E. R. Most, L. R. Weih, L. Rezzolla, and J. Schaffner-Bielich, *Phys. Rev. Lett.* **120**, 261103 (2018), arXiv:1803.00549 [gr-qc].
- [29] B. P. Abbott et al. (LIGO Scientific, Virgo), *Phys. Rev. Lett.* **121**, 161101 (2018), arXiv:1805.11581 [gr-qc].
- [30] A. Bauswein, O. Just, H.-T. Janka, and N. Stergioulas, *Astrophys. J. Lett.* **850**, L34 (2017), arXiv:1710.06843 [astro-ph.HE].
- [31] B. Margalit and B. D. Metzger, *Astrophys. J. Lett.* **850**, L19 (2017), arXiv:1710.05938 [astro-ph.HE].
- [32] L. Rezzolla, E. R. Most, and L. R. Weih, *Astrophys. J. Lett.* **852**, L25 (2018), arXiv:1711.00314 [astro-ph.HE].
- [33] M. Ruiz, S. L. Shapiro, and A. Tsokaros, *Phys. Rev. D* **97**, 021501 (2018), arXiv:1711.00473 [astro-ph.HE].
- [34] M. Shibata, E. Zhou, K. Kiuchi, and S. Fujibayashi, *Phys. Rev. D* **100**, 023015 (2019), arXiv:1905.03656 [astro-ph.HE].
- [35] A. Nathanail, E. R. Most, and L. Rezzolla, *Astrophys. J. Lett.* **908**, L28 (2021), arXiv:2101.01735 [astro-ph.HE].
- [36] H. Tan, J. Noronha-Hostler, and N. Yunes, *Phys. Rev. Lett.* **125**, 261104 (2020), arXiv:2006.16296 [astro-ph.HE].
- [37] E. R. Most, L. J. Papenfort, L. R. Weih, and L. Rezzolla, *Mon. Not. Roy. Astron. Soc.* **499**, L82 (2020), arXiv:2006.14601 [astro-ph.HE].
- [38] F. J. Fattoyev, C. J. Horowitz, J. Piekarewicz, and B. Reed, *Phys. Rev. C* **102**, 065805 (2020), arXiv:2007.03799 [nucl-th].
- [39] C. Cutler et al., *Phys. Rev. Lett.* **70**, 2984 (1993), arXiv:astro-ph/9208005.
- [40] M. Shibata, *Phys. Rev. Lett.* **94**, 201101 (2005), arXiv:gr-qc/0504082.
- [41] A. Bauswein and H. T. Janka, *Phys. Rev. Lett.* **108**, 011101 (2012), arXiv:1106.1616 [astro-ph.SR].
- [42] A. Bauswein, H. T. Janka, K. Hebeler, and A. Schwenk, *Phys. Rev. D* **86**, 063001 (2012), arXiv:1204.1888 [astro-ph.SR].
- [43] K. Takami, L. Rezzolla, and L. Baiotti, *Phys. Rev. D* **91**, 064001 (2015), arXiv:1412.3240 [gr-qc].
- [44] K. Takami, L. Rezzolla, and L. Baiotti, *Phys. Rev. Lett.* **113**, 091104 (2014), arXiv:1403.5672 [gr-qc].
- [45] S. Bernuzzi, A. Nagar, T. Dietrich, and T. Damour, *Phys. Rev. Lett.* **114**, 161103 (2015), arXiv:1412.4553 [gr-qc].
- [46] L. Rezzolla and K. Takami, *Phys. Rev. D* **93**, 124051 (2016), arXiv:1604.00246 [gr-qc].
- [47] S. Vretinaris, N. Stergioulas, and A. Bauswein, *Phys. Rev. D* **101**, 084039 (2020), arXiv:1910.10856 [gr-qc].
- [48] M. Breschi, S. Bernuzzi, K. Chakravarti, A. Camilletti, A. Prakash, and A. Perego, *Phys. Rev. D* **109**, 064009 (2024), arXiv:2205.09112 [gr-qc].
- [49] K. Topolski, S. D. Tootle, and L. Rezzolla, *Astrophys. J.* **960**, 86 (2024), arXiv:2310.10728 [gr-qc].
- [50] C. A. Raithel and E. R. Most, *Astrophys. J. Lett.* **933**, L39 (2022), arXiv:2201.03594 [astro-ph.HE].
- [51] E. R. Most, L. J. Papenfort, V. Dexheimer, M. Hanauske, S. Schramm, H. Stöcker, and L. Rezzolla, *Phys. Rev. Lett.* **122**, 061101 (2019), arXiv:1807.03684 [astro-ph.HE].
- [52] A. Bauswein, N.-U. F. Bastian, D. B. Blaschke, K. Chatziioannou, J. A. Clark, T. Fischer, and M. Oertel, *Phys. Rev. Lett.* **122**, 061102 (2019), arXiv:1809.01116 [astro-ph.HE].
- [53] E. R. Most, L. Jens Papenfort, V. Dexheimer, M. Hanauske, H. Stoecker, and L. Rezzolla, *Eur. Phys. J. A* **56**, 59 (2020), arXiv:1910.13893 [astro-ph.HE].
- [54] L. R. Weih, M. Hanauske, and L. Rezzolla, *Phys. Rev. Lett.* **124**, 171103 (2020), arXiv:1912.09340 [gr-qc].
- [55] S. L. Liebling, C. Palenzuela, and L. Lehner, *Class. Quant. Grav.* **38**, 115007 (2021), arXiv:2010.12567 [gr-qc].
- [56] A. Prakash, D. Radice, D. Logoteta, A. Perego, V. Nedora, I. Bombaci, R. Kashyap, S. Bernuzzi, and A. Endrizzi, *Phys. Rev. D* **104**, 083029 (2021), arXiv:2106.07885 [astro-ph.HE].
- [57] Y.-J. Huang, L. Baiotti, T. Kojo, K. Takami, H. Sotani, H. Togashi, T. Hatsuda, S. Nagataki, and Y.-Z. Fan, *Phys. Rev. Lett.* **129**, 181101 (2022), arXiv:2203.04528 [astro-ph.HE].
- [58] M. Ujevic, H. Gieg, F. Schianchi, S. V. Chaurasia, I. Tews, and T. Dietrich, *Phys. Rev. D* **107**, 024025 (2023), arXiv:2211.04662 [gr-qc].
- [59] A. Bauswein, H. T. Janka, and R. Oechslin, *Phys. Rev. D* **82**, 084043 (2010), arXiv:1006.3315 [astro-ph.SR].
- [60] A. Perego, S. Bernuzzi, and D. Radice, *Eur. Phys. J. A* **55**, 124 (2019), arXiv:1903.07898 [gr-qc].
- [61] A. Figura, J. J. Lu, G. F. Burgio, Z. H. Li, and H. J. Schulze, *Phys. Rev. D* **102**, 043006 (2020), arXiv:2005.08691 [gr-qc].
- [62] C. Raithel, V. Paschalidis, and F. Özel, *Phys. Rev. D* **104**, 063016 (2021), arXiv:2104.07226 [astro-ph.HE].
- [63] J. Fields, A. Prakash, M. Breschi, D. Radice, S. Bernuzzi, and A. da Silva Schneider, *Astrophys. J. Lett.* **952**, L36 (2023), arXiv:2302.11359 [astro-ph.HE].
- [64] C. A. Raithel and V. Paschalidis, *Phys. Rev. D* **110**, 043002 (2024), arXiv:2312.14046 [astro-ph.HE].
- [65] C. A. Raithel and V. Paschalidis, *Phys. Rev. D* **108**, 083029 (2023), arXiv:2306.13144 [astro-ph.HE].
- [66] V. Villa-Ortega, A. Lorenzo-Medina, J. Calderón Bustillo, M. Ruiz, D. Guerra, P. Cerdá-Duran, and J. A. Font, (2023), arXiv:2310.20378 [gr-qc].
- [67] M. Miravet-Tenés, D. Guerra, M. Ruiz, P. Cerdá-Durán, and J. A. Font, (2024), arXiv:2401.02493 [gr-qc].
- [68] Y. Sekiguchi, K. Kiuchi, K. Kyutoku, and M. Shibata, *Phys. Rev. Lett.* **107**, 211101 (2011), arXiv:1110.4442 [astro-ph.HE].
- [69] D. Radice, S. Bernuzzi, W. Del Pozzo, L. F. Roberts, and C. D. Ott, *Astrophys. J. Lett.* **842**, L10 (2017), arXiv:1612.06429 [astro-ph.HE].

- [70] S. Blacker, H. Kochankovski, A. Bauswein, A. Ramos, and L. Tolos, *Phys. Rev. D* **109**, 043015 (2024), [arXiv:2307.03710](https://arxiv.org/abs/2307.03710) [astro-ph.HE].
- [71] M. G. Alford, L. Bovard, M. Hanauske, L. Rezzolla, and K. Schwenzer, *Phys. Rev. Lett.* **120**, 041101 (2018), [arXiv:1707.09475](https://arxiv.org/abs/1707.09475) [gr-qc].
- [72] E. R. Most, S. P. Harris, C. Plumberg, M. G. Alford, J. Noronha, J. Noronha-Hostler, F. Pretorius, H. Witek, and N. Yunes, *Mon. Not. Roy. Astron. Soc.* **509**, 1096 (2021), [arXiv:2107.05094](https://arxiv.org/abs/2107.05094) [astro-ph.HE].
- [73] F. Zappa, S. Bernuzzi, D. Radice, and A. Perego, (2022), [10.1093/mnras/stad107](https://doi.org/10.1093/mnras/stad107), [arXiv:2210.11491](https://arxiv.org/abs/2210.11491) [astro-ph.HE].
- [74] P. L. Espino, P. Hammond, D. Radice, S. Bernuzzi, R. Gamba, F. Zappa, L. F. Longo Micchi, and A. Perego, *Phys. Rev. Lett.* **132**, 211001 (2024), [arXiv:2311.00031](https://arxiv.org/abs/2311.00031) [astro-ph.HE].
- [75] E. R. Most, A. Haber, S. P. Harris, Z. Zhang, M. G. Alford, and J. Noronha, *Astrophys. J. Lett.* **967**, L14 (2024), [arXiv:2207.00442](https://arxiv.org/abs/2207.00442) [astro-ph.HE].
- [76] M. Alford, A. Harutyunyan, and A. Sedrakian, *Phys. Rev. D* **104**, 103027 (2021), [arXiv:2108.07523](https://arxiv.org/abs/2108.07523) [astro-ph.HE].
- [77] S. P. Harris, B. Fore, and S. Reddy, (2024), [arXiv:2407.18890](https://arxiv.org/abs/2407.18890) [nucl-th].
- [78] B. Fore and S. Reddy, *Phys. Rev. C* **101**, 035809 (2020), [arXiv:1911.02632](https://arxiv.org/abs/1911.02632) [astro-ph.HE].
- [79] E. Loffredo, A. Perego, D. Logoteta, and M. Branchesi, *Astronomy & Astrophysics* **672**, A124 (2023), [arXiv:2209.04458](https://arxiv.org/abs/2209.04458) [astro-ph.HE].
- [80] V. Vijayan, N. Rahman, A. Bauswein, G. Martínez-Pinedo, and I. L. Arbina, *Physical Review D* **108**, 023020 (2023), [arXiv:2302.12055](https://arxiv.org/abs/2302.12055) [astro-ph.HE].
- [81] R. Bollig, H. T. Janka, A. Lohs, G. Martínez-Pinedo, C. J. Horowitz, and T. Melson, *Phys. Rev. Lett.* **119**, 242702 (2017), [arXiv:1706.04630](https://arxiv.org/abs/1706.04630) [astro-ph.HE].
- [82] G. Guo, G. Martínez-Pinedo, A. Lohs, and T. Fischer, *Phys. Rev. D* **102**, 023037 (2020), [arXiv:2006.12051](https://arxiv.org/abs/2006.12051) [hep-ph].
- [83] T. Fischer, G. Guo, G. Martínez-Pinedo, M. Liebendörfer, and A. Mezzacappa, *Phys. Rev. D* **102**, 123001 (2020), [arXiv:2008.13628](https://arxiv.org/abs/2008.13628) [astro-ph.HE].
- [84] H. Gieg, F. Schianchi, M. Ujevic, and T. Dietrich, (2024), [arXiv:2409.04420](https://arxiv.org/abs/2409.04420) [gr-qc].
- [85] A. Endrizzi, A. Perego, F. M. Fabbri, L. Branca, D. Radice, S. Bernuzzi, B. Giacomazzo, F. Pedrivera, and A. Lovato, *Eur. Phys. J. A* **56**, 15 (2020), [arXiv:1908.04952](https://arxiv.org/abs/1908.04952) [astro-ph.HE].
- [86] F. X. Timmes and D. Arnett, *The Astrophysical Journal Supplement Series* **125**, 277 (1999).
- [87] Equation (3.11.4) of https://www.pas.rochester.edu/~stte/phy418S21/units/unit_3-11.pdf.
- [88] K. S. Thorne and R. D. Blandford, *Modern Classical Physics: Optics, Fluids, Plasmas, Elasticity, Relativity, and Statistical Physics* (2017).
- [89] J. D. Kaplan, C. D. Ott, E. P. O'Connor, K. Kiuchi, L. Roberts, and M. Duez, *Astrophys. J.* **790**, 19 (2014), [arXiv:1306.4034](https://arxiv.org/abs/1306.4034) [astro-ph.HE].
- [90] Equation (3.8.19) of https://www.pas.rochester.edu/~stte/phy418S21/units/unit_3-11.pdf.
- [91] S. A. Bludman and K. A. van Riper, *Astrophys. J.* **212**, 859 (1977).
- [92] A. Perego, S. Bernuzzi, and D. Radice, *European Physical Journal A* **55**, 124 (2019), [arXiv:1903.07898](https://arxiv.org/abs/1903.07898) [gr-qc].
- [93] S. A. Bludman and K. A. van Riper, *Astrophys. J.* **224**, 631 (1978).
- [94] A. W. Steiner, M. Hempel, and T. Fischer, *Astrophys. J.* **774**, 17 (2013), [arXiv:1207.2184](https://arxiv.org/abs/1207.2184) [astro-ph.SR].
- [95] M. Hempel and J. Schaffner-Bielich, *Nucl. Phys. A* **837**, 210 (2010), [arXiv:0911.4073](https://arxiv.org/abs/0911.4073) [nucl-th].
- [96] S. Typel, *Phys. Rev. C* **71**, 064301 (2005), [arXiv:nucl-th/0501056](https://arxiv.org/abs/nucl-th/0501056).
- [97] S. Typel, G. Ropke, T. Klahn, D. Blaschke, and H. H. Wolter, *Phys. Rev. C* **81**, 015803 (2010), [arXiv:0908.2344](https://arxiv.org/abs/0908.2344) [nucl-th].
- [98] P. Hammond, I. Hawke, and N. Andersson, *Phys. Rev. D* **104**, 103006 (2021), [arXiv:2108.08649](https://arxiv.org/abs/2108.08649) [astro-ph.HE].
- [99] R. C. Tolman, *Physical Review* **55**, 364 (1939).
- [100] J. R. Oppenheimer and G. M. Volkoff, *Phys. Rev.* **55**, 374 (1939).
- [101] stellarcollapse.org.
- [102] A. W. Steiner, “O2scl: Object-oriented scientific computing library,” Astrophysics Source Code Library, record ascl:1408.019 (2014).
- [103] M. D. Duez, Y. T. Liu, S. L. Shapiro, and B. C. Stephens, *Phys. Rev. D* **72**, 024028 (2005), [arXiv:astro-ph/0503420](https://arxiv.org/abs/astro-ph/0503420).
- [104] S. Bernuzzi and D. Hilditch, *Phys. Rev. D* **81**, 084003 (2010), [arXiv:0912.2920](https://arxiv.org/abs/0912.2920) [gr-qc].
- [105] D. Hilditch, S. Bernuzzi, M. Thierfelder, Z. Cao, W. Tichy, and B. Bruegmann, *Phys. Rev. D* **88**, 084057 (2013), [arXiv:1212.2901](https://arxiv.org/abs/1212.2901) [gr-qc].
- [106] E. R. Most, L. J. Papenfort, and L. Rezzolla, *Mon. Not. Roy. Astron. Soc.* **490**, 3588 (2019), [arXiv:1907.10328](https://arxiv.org/abs/1907.10328) [astro-ph.HE].
- [107] Z. B. Etienne, V. Paschalidis, R. Haas, P. Mösta, and S. L. Shapiro, *Class. Quant. Grav.* **32**, 175009 (2015), [arXiv:1501.07276](https://arxiv.org/abs/1501.07276) [astro-ph.HE].
- [108] F. Löffler et al., *Class. Quant. Grav.* **29**, 115001 (2012), [arXiv:1111.3344](https://arxiv.org/abs/1111.3344) [gr-qc].
- [109] L. Del Zanna, O. Zanotti, N. Bucciantini, and P. Londrillo, *Astron. Astrophys.* **473**, 11 (2007), [arXiv:0704.3206](https://arxiv.org/abs/0704.3206) [astro-ph].
- [110] Y. Zlochower, J. G. Baker, M. Campanelli, and C. O. Lousto, *Phys. Rev. D* **72**, 024021 (2005), [arXiv:gr-qc/0505055](https://arxiv.org/abs/gr-qc/0505055).
- [111] R. Borges, M. Carmona, B. Costa, and W. S. Don, *Journal of computational physics* **227**, 3191 (2008).
- [112] W. Kastaun, J. V. Kalinani, and R. Ciolfi, *Phys. Rev. D* **103**, 023018 (2021), [arXiv:2005.01821](https://arxiv.org/abs/2005.01821) [gr-qc].
- [113] E. Schnetter, S. H. Hawley, and I. Hawke, *Class. Quant. Grav.* **21**, 1465 (2004), [arXiv:gr-qc/0310042](https://arxiv.org/abs/gr-qc/0310042).
- [114] E. R. Most and C. A. Raithel, *Phys. Rev. D* **104**, 124012 (2021), [arXiv:2107.06804](https://arxiv.org/abs/2107.06804) [astro-ph.HE].
- [115] P. Grandclement, *J. Comput. Phys.* **229**, 3334 (2010), [arXiv:0909.1228](https://arxiv.org/abs/0909.1228) [gr-qc].
- [116] L. J. Papenfort, S. D. Tootle, P. Grandclement, E. R. Most, and L. Rezzolla, *Phys. Rev. D* **104**, 024057 (2021), [arXiv:2103.09911](https://arxiv.org/abs/2103.09911) [gr-qc].
- [117] H. P. Pfeiffer and J. W. York, Jr., *Phys. Rev. D* **67**, 044022 (2003), [arXiv:gr-qc/0207095](https://arxiv.org/abs/gr-qc/0207095).
- [118] W. Tichy, *Phys. Rev. D* **84**, 024041 (2011), [arXiv:1107.1440](https://arxiv.org/abs/1107.1440) [gr-qc].
- [119] E. R. Most, L. J. Papenfort, S. Tootle, and L. Rezzolla, *Astrophys. J.* **912**, 80 (2021), [arXiv:2012.03896](https://arxiv.org/abs/2012.03896) [astro-ph.HE].
- [120] L. J. Papenfort, E. R. Most, S. Tootle, and L. Rezzolla, *Mon. Not. Roy. Astron. Soc.* **513**, 3646 (2022),

- arXiv:2201.03632 [astro-ph.HE].
- [121] S. D. Tootle, L. J. Papenfort, E. R. Most, and L. Rezzolla, *Astrophys. J. Lett.* **922**, L19 (2021), arXiv:2109.00940 [gr-qc].
- [122] B. D. Metzger, *Living Rev. Rel.* **20**, 3 (2017), arXiv:1610.09381 [astro-ph.HE].
- [123] L. Bovard and L. Rezzolla, *Class. Quant. Grav.* **34**, 215005 (2017), arXiv:1705.07882 [gr-qc].
- [124] F. Foucart, P. Moesta, T. Ramirez, A. J. Wright, S. Darbha, and D. Kasen, *Phys. Rev. D* **104**, 123010 (2021), arXiv:2109.00565 [astro-ph.HE].
- [125] L. Bovard, D. Martin, F. Guercilena, A. Arcones, L. Rezzolla, and O. Korobkin, *Phys. Rev. D* **96**, 124005 (2017), arXiv:1709.09630 [gr-qc].
- [126] V. Nedora, D. Radice, S. Bernuzzi, A. Perego, B. Daszuta, A. Endrizzi, A. Prakash, and F. Sichi-anchi, *Mon. Not. Roy. Astron. Soc.* **506**, 5908 (2021), arXiv:2104.04537 [astro-ph.HE].
- [127] A. Bauswein, S. Gorieli, and H.-T. Janka, *The Astrophysical Journal* **773**, 78 (2013).
- [128] N. T. Bishop and L. Rezzolla, *Living Rev. Rel.* **19**, 2 (2016), arXiv:1606.02532 [gr-qc].
- [129] C. Reisswig and D. Pollney, *Class. Quant. Grav.* **28**, 195015 (2011), arXiv:1006.1632 [gr-qc].
- [130] K. Chatziioannou, J. A. Clark, A. Bauswein, M. Millhouse, T. B. Littenberg, and N. Cornish, *Phys. Rev. D* **96**, 124035 (2017), arXiv:1711.00040 [gr-qc].
- [131] M. Wijngaarden, K. Chatziioannou, A. Bauswein, J. A. Clark, and N. J. Cornish, *Phys. Rev. D* **105**, 104019 (2022), arXiv:2202.09382 [gr-qc].
- [132] A. W. Criswell, J. Miller, N. Woldemariam, T. Soultanis, A. Bauswein, K. Chatziioannou, M. W. Coughlin, G. Jones, and V. Mandic, *Phys. Rev. D* **107**, 043021 (2023), arXiv:2211.05250 [astro-ph.HE].
- [133] M. Breschi, R. Gamba, S. Borhanian, G. Carullo, and S. Bernuzzi, (2022), arXiv:2205.09979 [gr-qc].
- [134] M. Breschi, G. Carullo, and S. Bernuzzi, (2023), arXiv:2301.09672 [gr-qc].
- [135] L. Barsotti, P. Fritschel, M. Evans, and S. Gras, LIGO Document T1800044-v5, Tech. Rep. (LVK Collaboration, 2010).
- [136] F. Foucart, *Mon. Not. Roy. Astron. Soc.* **475**, 4186 (2018), arXiv:1708.08452 [astro-ph.HE].
- [137] D. Radice, S. Bernuzzi, A. Perego, and R. Haas, *Mon. Not. Roy. Astron. Soc.* **512**, 1499 (2022), arXiv:2111.14858 [astro-ph.HE].
- [138] M. R. Izquierdo, J. F. Abalos, and C. Palenzuela, *Phys. Rev. D* **109**, 043044 (2024), arXiv:2312.09275 [astro-ph.HE].
- [139] M. Diamond, D. F. G. Fiorillo, G. Marques-Tavares, I. Tamborra, and E. Vitagliano, *Phys. Rev. Lett.* **132**, 101004 (2024), arXiv:2305.10327 [hep-ph].
- [140] C. A. Manzari, Y. Park, B. R. Safdi, and I. Savoray, (2024), arXiv:2405.19393 [hep-ph].
- [141] J. D. Hunter, *Computing in Science & Engineering* **9**, 90 (2007).
- [142] C. R. Harris, K. J. Millman, S. J. van der Walt, R. Gommers, P. Virtanen, D. Cournapeau, E. Wieser, J. Taylor, S. Berg, N. J. Smith, R. Kern, M. Picus, S. Hoyer, M. H. van Kerkwijk, M. Brett, A. Haldane, J. F. del Río, M. Wiebe, P. Peterson, P. Gérard-Marchant, K. Sheppard, T. Reddy, W. Weckesser, H. Abbasi, C. Gohlke, and T. E. Oliphant, *Nature* **585**, 357 (2020).
- [143] P. Virtanen, R. Gommers, T. E. Oliphant, M. Haberland, T. Reddy, D. Cournapeau, E. Burovski, P. Peterson, W. Weckesser, J. Bright, S. J. van der Walt, M. Brett, J. Wilson, K. J. Millman, N. Mayorov, A. R. J. Nelson, E. Jones, R. Kern, E. Larson, C. J. Carey, Í. Polat, Y. Feng, E. W. Moore, J. VanderPlas, D. Laxalde, J. Perktold, R. Cimrman, I. Henriksen, E. A. Quintero, C. R. Harris, A. M. Archibald, A. H. Ribeiro, F. Pedregosa, P. van Mulbregt, and SciPy 1.0 Contributors, *Nature Methods* **17**, 261 (2020).
- [144] G. Bozzola, *The Journal of Open Source Software* **6**, 3099 (2021), arXiv:2104.06376 [gr-qc].